Magnetic reconnection plasmoid model for Sagittarius A* flares

N. Aimar, A. Dmytriiev, F.H. Vincent, I. El Mellah, T. Paumard, G. Perrin, A. Zech

A&A 672, A62 (2023)
https://doi.org/10.1051/0004-6361/202244936

Astronomy & Astrophysics

Magnetic reconnection plasmoid model for Sagittarius A* flares

N. Aimar[1], A. Dmytriiev[2], F. H. Vincent[1], I. El Mellah[3,5], T. Paumard[1], G. Perrin[1], and A. Zech[4]

[1] LESIA, Observatoire de Paris, Université PSL, CNRS, Sorbonne Université, Université Paris Cité, 5 place Jules Janssen, 92195 Meudon, France
e-mail: nicolas.aimar@obspm.fr
[2] Centre for Space Research, North-West University, Potchefstroom 2531, South Africa
[3] Univ. Grenoble Alpes, CNRS, IPAG, 38000 Grenoble, France
[4] LUTH, Observatoire de Paris, CNRS, Université Paris Diderot, 5 place Jules Janssen, 92190 Meudon, France
[5] Departamento de Física, Universidad de Santiago de Chile, Av. Victor Jara 3659, Santiago, Chile

Received 9 September 2022 / Accepted 27 January 2023

ABSTRACT

Context. Sagittarius A*, the supermassive black hole at the center of our Galaxy, exhibits episodic near-infrared flares. The recent monitoring of three such events with the GRAVITY instrument has shown that some flares are associated with orbital motions in the close environment of the black hole. The GRAVITY data analysis indicates a super-Keplerian azimuthal velocity, while (sub-) Keplerian velocity is expected for the hot flow surrounding the black hole.
Aims. We develop a semi-analytic model of the Sagittarius A* flares based on an ejected large plasmoid, inspired by recent particle-in-cell global simulations of black hole magnetospheres. We model the infrared astrometric and photometric signatures associated with this model.
Methods. We considered a spherical macroscopic hot plasma region that we call a large plasmoid. This structure was ejected along a conical orbit in the vicinity of the black hole. This plasmoid was assumed to be formed by successive mergers of smaller plasmoids produced through magnetic reconnection that we did not model. Nonthermal electrons were injected into the plasmoid. We computed the evolution of the electron-distribution function under the influence of synchrotron cooling. We solved the radiative transfer problem associated with this scenario and transported the radiation along null geodesics of the Schwarzschild space time. We also took the quiescent radiation of the accretion flow into account, on top of which the flare evolves.
Results. For the first time, we successfully account for the astrometric and flux variations of the GRAVITY data with a flare model that incorporates an explicit modeling of the emission mechanism. The prediction of our model and recent data agree well. In particular, the azimuthal velocity of the plasmoid is set by the magnetic field line to which it belongs, which is anchored in the inner parts of the accretion flow, hence the super-Keplerian motion. The astrometric track is also shifted with respect to the center of mass due to the quiescent radiation, in agreement with the difference measured with the GRAVITY data.
Conclusions. These results support the hypothesis that magnetic reconnection in a black hole magnetosphere is a viable model for the infrared flares of Sagittarius A* .

Key words. accretion, accretion disks – magnetic reconnection – black hole physics – relativistic processes – radiative transfer – radiation mechanisms: non-thermal

1. Introduction

The Galactic center hosts the compact radio source Sagittarius A* (Sgr A*) with an estimated mass of 4.297 million solar masses at a distance of only 8.277 kpc (GRAVITY Collaboration 2022). This makes the compact object associated with Sgr A* the closest supermassive black hole (SMBH) candidate to Earth. Sgr A* is a low-luminosity accretion flow with an accretion rate of $(5.2–9.5)\times10^{-9}\,M_\odot\,\mathrm{yr}^{-1}$ and a bolometric luminosity of $(6.8–9.2)\times10^{35}\,\mathrm{erg\,s}^{-1}$ (Bower et al. 2019; Event Horizon Telescope Collaboration 2022b) and thus is accreting at a highly sub-Eddington rate. It has been the subject of numerous observing campaigns over the past two decades that were conducted to test the massive black hole (MBH) paradigm (see GRAVITY Collaboration 2020b) and study the physics of radiatively inefficient accretion flows (RIAF) around an SMBH.

Sgr A* shows a slow and low-amplitude variability in radio (Lo et al. 1975; Backer 1978; Krichbaum et al. 1998; Falcke 1999; Bower et al. 2006; Michail et al. 2021b), in millimeter and submillimeter (Mauerhan et al. 2005; Macquart et al. 2006; Yusef-Zadeh et al. 2006; Marrone et al. 2008; Brinkerink et al. 2015; Wielgus et al. 2022a), but also high-amplitude and rapid variability in the near-infrared (NIR; Genzel et al. 2003; Ghez et al. 2004; Hornstein et al. 2007; Hora et al. 2014) and in X-rays (Baganoff et al. 2001; Nowak et al. 2012; Neilsen et al. 2013; Barrière et al. 2014; Ponti et al. 2015). The flux distribution in the NIR of Sgr A* has been the subject of numerous studies. Some claimed a single state modeled by red noise (Witzel et al. 2018; Do et al. 2019) for the variability of Sgr A* , while others claimed that there are two states for Sgr A* (Genzel et al. 2003; Dodds-Eden et al. 2011; GRAVITY Collaboration 2020a; Witzel et al. 2021): a continuously low-amplitude variable state called the quiescent state, and the flare state, which is described by short and bright flux with a typical timescale of 30 min to one hour with a rate of about four a day. Multiwavelength studies showed that when an X-ray flare is observed, a counterpart exists in the NIR, suggesting a common origin. The reverse is not true, however (Fazio et al. 2018). Moreover, the flare can also be observed in the submillimeter range, but with a time lag of several minutes (Eckart et al. 2008, 2009; Dodds-Eden et al. 2009;

Michail et al. 2021a; Witzel et al. 2021) following a dimming (Wielgus et al. 2022a; Ripperda et al. 2022).

Recently, the GRAVITY instrument (GRAVITY Collaboration 2017; Eisenhauer et al. 2008, 2011; Paumard et al. 2008) was able to resolve the motion of the NIR centroid during three bright flare events, showing a clockwise continuous rotation at low inclination close to face-on ($i \sim 20$ deg), consistent with an emission region that is located at a few gravitational radii $r_g = GM/c^2$ from the central black hole (GRAVITY Collaboration 2018). These flares are thus powered very close to the event horizon of the black hole. The exploration of a relativistic accretion region as close to the event horizon with high-precision astrometry and imaging techniques such as GRAVITY and the Event Horizon Telescope (EHT) (Event Horizon Telescope Collaboration 2022a) promises important information for physics and astronomy, including new tests of the MBH paradigm.

Significant efforts have been made to explain the flares of Sgr A*: red noise (Do et al. 2009), a hot spot (Hamaus et al. 2009; Genzel et al. 2003; Broderick & Loeb 2006), an ejected blob (Vincent et al. 2014), star-disk interaction (Nayakshin et al. 2004), and disk instability (Tagger & Melia 2006). The GRAVITY observations in 2018 (GRAVITY Collaboration 2018) support the hot spot model. However, the physical origin of these hot spots remains an open question. Instabilities in black hole accretion disks are a candidate, for instance, the triggering of Rossby wave instabilities (RWI; Tagger & Melia 2006; Vincent et al. 2014). Alternatively, it might originate from the dissipation of electromagnetic energy through magnetic reconnection. This modification of the magnetic field topology results from the inversion of the magnetic field orientation across a current sheet that eventually breaks into magnetic islands called plasmoids (Komissarov 2004, 2005; Komissarov & McKinney 2007; Loureiro et al. 2007; Sironi & Spitkovsky 2014; Parfrey et al. 2019; Ripperda et al. 2020; Porth et al. 2021). In past years, numerical simulations have repeatedly highlighted the ubiquity of magnetic reconnection in black hole (BH) magnetospheres, regardless of the physical point of view: global particle-in-cell (PIC) simulations in Kerr metrics (El Mellah et al. 2022; Crinquand et al. 2022), resistive general-relativistic magnetohydrodynamics (GRMHD) simulations (Ripperda et al. 2020; Dexter et al. 2020a,b), or resistive force-free simulations (Parfrey et al. 2015). PIC simulations show that magnetic reconnection in the collisionless corona of spinning BHs can accelerate leptons up to relativistic Lorentz factors of $\gamma \sim 10^{3...7}$ (El Mellah et al. 2022), which is sufficiently high to generate the variable IR (and X-ray) emission (Rowan et al. 2017; Werner et al. 2018; Ball et al. 2018; Zhang et al. 2021; Scepi et al. 2022).

The GRMHD and PIC frameworks each have different limitations. GRMHD simulations describe the evolution of the accretion flow over long timescales, typically about several 100 000 r_g/c, but they rely on a fluid representation. Consequently, they cannot self-consistently capture the kinetic effects that are important to constrain dissipation, particle acceleration, and subsequent nonthermal radiation. On the other hand, PIC simulations provide an accurate description of the microphysics, but at the cost of simulations that can only span a few $100 r_g/c$ in time and with a limited scale separation between global scales and plasma scales.

We developed a semi-analytical model that is fed by the knowledge accumulated by recent GRMHD and GRPIC simulations. The aim is to condense the complex physics of GRMHD and GRPIC models into a reasonably small set of simple parameters and thus allow probing a large parameter space within a reasonable computing time. We also wish to remain as agnostic as possible regarding the initial conditions of the flow. In this context, we discuss the interpretation of the GRAVITY Collaboration (2018) flare data and pay particular attention to the following diagnostics: (i) the marginally detected shift between the astrometric data and the location of the center of mass, (ii) the difference between the data and the hot-spot model used by GRAVITY Collaboration (2018), which assumes a Keplerian orbit and (iii) the physical origin of the rising and decaying phases of the flare light curve in the context of magnetic reconnection.

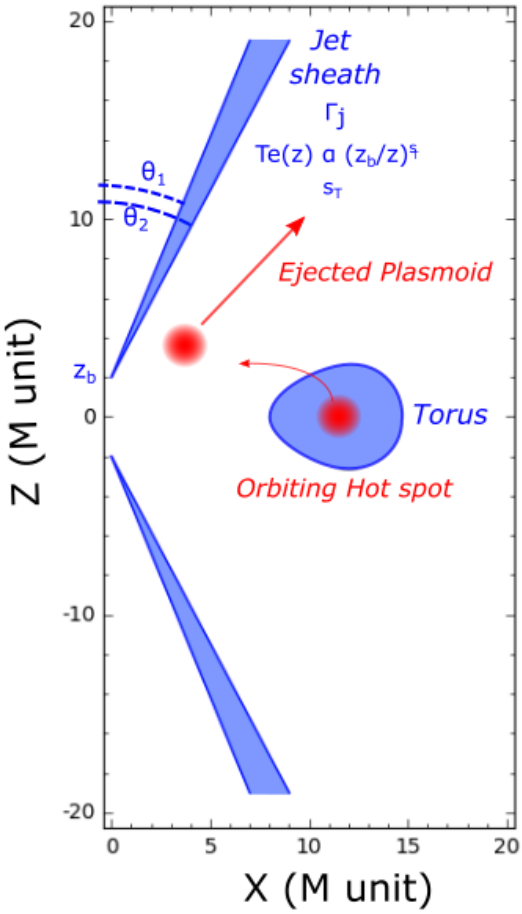

Fig. 1. Scheme of the torus-jet model for the quiescent state in blue and flares in red. Two trajectories are considered for the flare, which can either rotate in the torus (hot-spot model) or be ejected along the jet sheath (plasmoid model). The jet is parameterized by the angles θ_1 and θ_2, which describe the angular opening of the radiation-emitting sheath, by the base height z_b, the constant Lorentz factor Γ_j, and by the temperature power-law index s_T. The jet is symmetrical with respect to the equatorial plane, and it is axisymmetric.

The first point can be discussed in the context of a very simple hot-spot model and is the main topic of Sect. 2. Section 3 is the core of our study and focuses on the second and third points above. It presents a semi-analytical large plasmoid model that is the result of magnetic reconnection. It highlights in particular the impact of considering a self-consistent evolution of the electron distribution function through kinetic modeling. This section shows that our plasmoid model is able to reasonably account for the flare data of GRAVITY Collaboration (2018). The limitations of our plasmoid model are discussed in Sect. 4. The conclusions and perspectives are given in Sect. 5.

2. Quiescent flow impact on astrometry: Shifting and rotating the orbit

GRAVITY Collaboration (2018) used a hot-spot model in an equatorial circular orbit to fit the astrometry of three bright flares. They considered a constant radiation flux from the emitting region orbiting the black hole to fit the orbital motion. The effect of out-of-plane motion and orbital shear has also been studied by GRAVITY Collaboration (2020c) to model the flares. However, the impact of the quiescent radiation surrounding the hot spot was not taken into account. The aim of this section is to show that taking the quiescent radiation into account can lead to a shift and rotation of the orbit on sky. We note a 1σ difference between the center of the orbit of the hot spot and the center of mass derived from the orbit of S2 in GRAVITY Collaboration (2018), which makes this shift marginal.

In this section, we use a simplified hot-spot model that is sufficient to highlight the main effects of the quiescent radiation. This simple model also allows us to introduce the most important relativistic effects at play, which were already studied in many previous works (Broderick & Loeb 2006; Hamaus et al. 2009). These reminders will be helpful when we consider a more complex hot-spot model in Sect. 3, which is the main aim of this paper.

2.1. Simple hot-spot + quiescent model for the flaring Sgr A*

The quiescent radiation of Sgr A* was modeled by means of the torus-jet model as derived in Vincent et al. (2019), to which we refer for all details. Figure 1 shows the main features of the model. The torus emits thermal synchrotron radiation, while the flux emitted by the jet follows a κ distribution (i.e., a thermal core with a power-law tail). The multiwavelength spectrum of the quiescent Sgr A* is well fit with this model. The κ distribution emission from the jets dominates at most wavelengths, except at the submillimeter bump, where the flux mostly comes from the thermal disk. We summarize the best-fit parameters in Table 1, and the resulting best-fit quiescent spectrum is given in Fig. 2. More details of the fitting procedure are given in Appendix A. With these parameters, the flux of the torus-jet model at 2.2 µm is 1.1 mJy. This perfectly agrees with the median quiescent dereddened flux provided by GRAVITY Collaboration (2020a) of 1.1 ± 0.3 mJy. At this wavelength, the torus is optically thin and its emission is negligible compared to the jet. In the remainder of this paper, where we focus on the infrared band, we therefore neglect the torus and consider a pure jet quiescent model, unless otherwise noted.

The only relevant features of our quiescent model for the rest of this paper are the location of its infrared centroid and its NIR flux. As depicted in the right panel of Fig. 2, the centroid of our jet-dominated model lies very close to the mass center. We verified that considering a disk-dominated model changes the position of the quiescent centroid at low inclination only very marginally (see the blue and green dots in the left panel of Fig. 3). Our conclusions are thus not biased by our particular choice of a jet-dominated quiescent model.

The hot-spot model is composed of a plasma sphere of radius $1\,r_g$ (fixed) with a uniform but time-dependent κ-distribution for the electrons. The emissivity j_ν and absorptivity α_ν coefficients depend on the density, temperature, and magnetic field, which we considered uniform. We used the fitting formula of Pandya et al. (2016) to compute these coefficients. The typical light curve of a flare is characterized by a phase with increasing and another phase with decreasing flux. We modeled this behavior by a Gaussian time modulation on the density and temperature as follows:

$$n_e(t) = n_e^{hs}\ \exp\left(-0.5 \times \left(\frac{t - t_{ref}}{t_\sigma}\right)^2\right), \quad (1)$$

$$T_e(t) = T_e^{hs}\ \exp\left(-0.5 \times \left(\frac{t - t_{ref}}{t_\sigma}\right)^2\right), \quad (2)$$

where t_σ is the typical duration of the flare. As n_e varies over time (Eq. (1)), the magnetic field strength also varies because we set a constant magnetization $\sigma = B^2/4\pi m_p c^2 n_e$.

In contrast to GRAVITY Collaboration (2020c), we kept the circular equatorial orbit of GRAVITY Collaboration (2018) as we assumed that the hot spot is formed in the equatorial plane, and we did not take any shearing effect into account and assumed a constant spherical geometry of the hot spot. We summarize all the input parameters of the hot spot in Table 2.

Table 1. Best-fit parameters of the torus+jet quiescent model.

Parameter	Symbol	Value
Black Hole		
Mass [$M_\odot$]	M	4.297×10^6
Distance [kpc]	d	8.277
Spin	a	0
Inclination [deg]	i	20
Torus		
Angular momentum [r_g/c]	l	4
Inner radius [r_g]	r_{in}	8
Polytropic index	k	5/3
Central density [cm^{-3}]	n_e^T	1.2×10^9
Central temperature [K]	T_e^T	7×10^9
Magnetization parameter	σ^T	0.002
Jet		
Inner opening angle [deg]	θ_1	20
Outer opening angle [deg]	θ_2	$\theta_1 + 3.5$
Jet base height [r_g]	z_b	2
Bulk Lorentz factor	Γ_j	1.15
Base number density [cm^{-3}]	n_e^J	3.5×10^6
Base temperature [K]	T_e^J	3×10^{10}
Temperature slope	s_T	0.21
κ index	κ^J	5.5
Magnetization parameter	σ^J	(fixed) 1

Notes. We kept the same geometrical parameters, bulk Lorentz factor, and κ-index as Vincent et al. (2019), and we fit the base number density, base temperature, and temperature slope of the jet considering the correction (see bellow) and the new value of the jet magnetization parameter. The parameters of the torus are unchanged.

2.2. Shifting the orbit on sky

Figure 3 shows the impact of taking the quiescent radiation into account on the astrometry of the flare, considering the trivial case of a constant-emission hot spot, as well as the varying-emission hot spot introduced in Sect. 2.1.

Regardless of whether the intrinsic emission of the hot spot varies, the first effect of adding a quiescent radiation clearly is to shrink the orbit size because the overall centroid is moved toward the quiescent radiation centroid, which always lies close to the mass center. A slightly less obvious effect is that when the hot-spot emission varies in time, the orbit can shift in the plane of sky

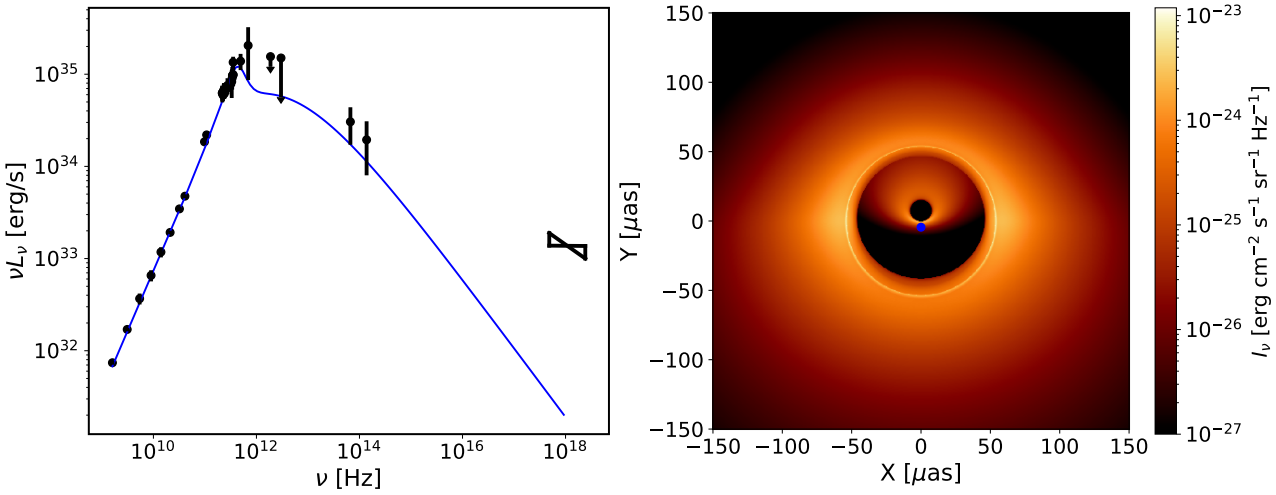

Fig. 2. Our torus-jet model for the quiescent state of Sgr A*. Left: spectrum associated with the best fit of the torus-jet model (see Table 1) for the quiescent state of Sgr A* ($\chi^2_{\rm red} = 0.91$ with nd.o.f. = 27). The data are taken from Bower et al. (2015) for $\nu < 50$ GHz, Brinkerink et al. (2015) for the two points around 100 GHz, Liu et al. (2016) for the 492 GHz point, Marrone et al. (2006) for the 690 GHz point, von Fellenberg et al. (2018) for the far-infrared upper limits, Witzel et al. (2018) for the mid-infrared data, and Baganoff et al. (2001) for the X-ray bow-tie. We note that as in Vincent et al. (2019), the X-ray data were not fit as we did not take bremsstrahlung or Comptonized emission into account. Right: best-fit image at 2.2 µm of the torus-jet model with a field of view of 150 µas seen with an inclination of 20 deg and a PALN of π rad. The color bar gives the values of the specific intensity in cgs units in log-scale. The outer region emission comes from the backward jet, and the emission close to the center comes from the forward part of the jet. The centroid of the jet is represented by the blue dot at ∼(0, −2.2).

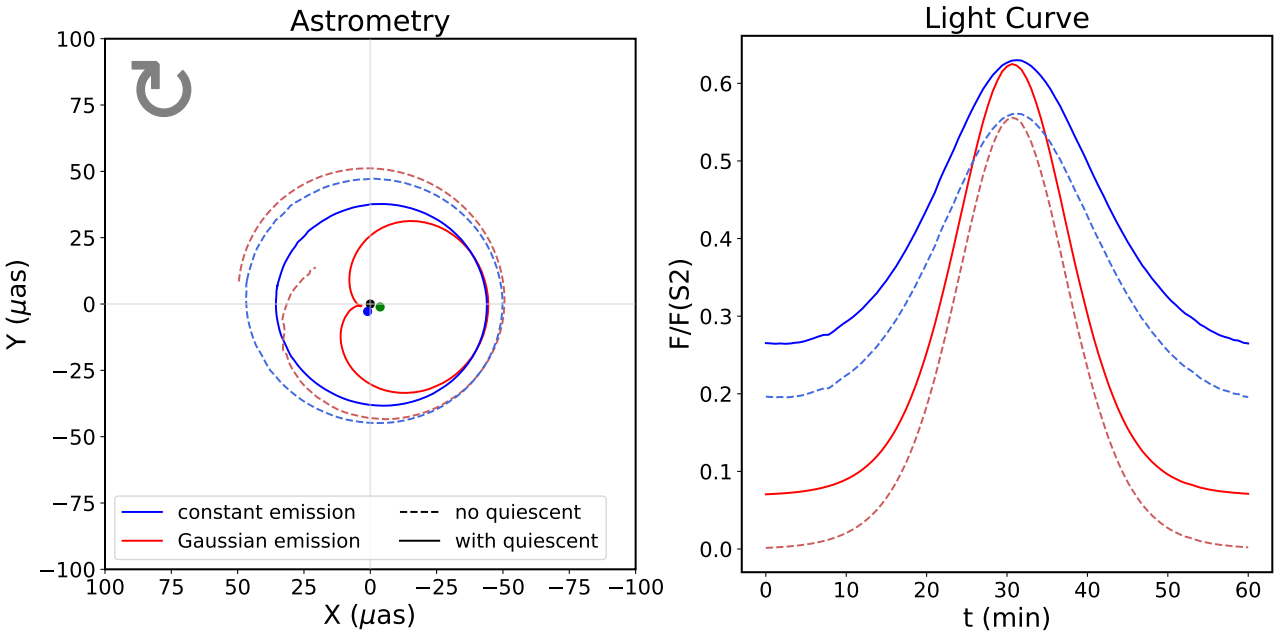

Fig. 3. Astrometry (left) and light curves (right) of the hot spot – jet model with two values for the quiescent state corresponding to no quiescent (dashed lines) and the with quiescent state (full lines). In shades of blue, the hot spot has a nearly constant emission ($t_\sigma \gg t_{\rm orbit}$). The effect of beaming is reflected in the light curves. In shades of red, the hot spot has a Gaussian time emission with $t_\sigma = 30$ min. The parameters of the hot spot are listed in Table 2. We synchronized the beaming and intrinsic maximum of the Gaussian modulation. The black, blue, and green dots in the left panels represent the position of Sgr A*, the jet centroid, and the disk centroid, respectively.

and is no longer centered at the location of the center of mass. This is clearly apparent for the solid red orbit in the left panel of Fig. 3. The reason is the time variation of the intensity ratio between the quiescent and the hot-spot radiation. At early and late times, the hot spot has a weaker emission than the quiescent component, and the overall centroid coincides with the quiescent centroid. As the hot-spot emission increases and dominates, the overall centroid will be driven toward it. This shift between the astrometric data and the position of the center of mass is visible at 1σ significance in the data of GRAVITY Collaboration (2018).

We note another nontrivial effect that appears in the varying-emission hot-spot orbit without any quiescent radiation (dotted red orbit in Fig. 3). The orbit is not closing because of the time delay between the primary and secondary images. At the end of the simulation, the flux from the secondary image is intrinsically

Table 2. Summary of parameters of the hot-spot model.

Parameter	Symbol	Value
Hot spot		
Number density max [cm^{-3}]	n_e^{hs}	1.05×10^7
Temperature max [K]	T_e^{hs}	9.03×10^{10}
Time Gaussian sigma [min]	t_σ	30
Magnetization parameter	σ^{hs}	0.01
κ-distribution index	κ^{hs}	5
Orbital radius [r_g]	R^{hs}	9
Initial azimuth angle [deg]	φ_0^{hs}	90
PALN [deg]	Ω	160

Notes. We used the maximum number density and temperature of the best-fit jet in Table 1 as reference and scaled them for the hot spot by a factor 3.01. PALN is the position angle of the line of nodes.

higher than that of the primary (the emission times of the primary and secondary are different), and it is amplified by the beaming effect. When the centroid is computed, the secondary image has a stronger impact at this time than before, resulting in a closer centroid position relative to the black hole. This astrometric impact of the secondary image was discussed by Hamaus et al. (2009).

2.3. Rotating the orbit on sky

It is difficult to disentangle the intrinsic time variability of the hot spot from the variability that is due to the relativistic beaming effect. Figure 4 illustrates the impact on astrometry and light curve of varying the relative influence between the intrinsic and beaming-related variability. Here, we changed the initial azimuthal coordinate φ_0 of the hot spot along its orbit, in order to change the dephasing between the time of the maximum intrinsic emission ($t = t_{ref}$), which is fixed, and the time of the maximum constructive beaming effect (when the hot spot moves toward the observer). The orbit rotates around the quiescent centroid following the variation in φ_0 (left panel of Fig. 4). The light curve is also strongly affected. It reaches much brighter levels when the intrinsic emission maximum is in phase with the constructive beaming effect.

We show that the quiescent state of Sgr A* can have a significant impact on the observed astrometry by shrinking the apparent orbit, creating a shift between the center of the latter and the position of the mass center. These effects must be kept in mind for the comparison to the flare data at the end of the following section.

3. Plasmoid model from magnetic reconnection

In this section, we develop a semi-analytical hot-spot-like model in order to interpret the rise and decay of Sgr A* flares. We therefore proceed with respect to the model we used in Sect. 2, where a Gaussian modulation of the emission was enforced without physical motivation.

Black hole magnetospheres naturally lead to the development of equatorial current sheets corresponding to a strong spatial gradient of the magnetic field, which changes sign at the equator (Komissarov 2004; Komissarov & McKinney 2007; Parfrey et al. 2019; Ripperda et al. 2020). This configuration results in magnetic reconnection, that is, in a change of the topology of the field lines forming X points (Komissarov 2005; Loureiro et al. 2007; Sironi & Spitkovsky 2014). This process is intrinsically nonideal and thus can only be captured by either resistive MHD or kinetic simulations. For suitable values of the magnetic diffusivity, the reconnecting current sheet can break into chains of plasmoids, that is, magnetic islands separated by X points (Loureiro et al. 2007; Parfrey et al. 2019; Ripperda et al. 2020; Porth et al. 2021).

The reconnection rate (i.e., the typical rate at which magnetic energy is dissipated into particle kinetic energy) is equal to the ratio v_{rec}/v_{out}, with v_{rec} the velocity of matter injected into the reconnection region, and v_{out} the bulk outflow velocity of particles accelerated by the reconnection event. The outflow velocity is approximately the Alfvén speed, $v_{out} \approx v_A$, which is itself approximately the speed of light, $v_A \approx c$, for strongly magnetized environments. The reconnection rate has been shown to be rather independent of the details of the chosen parameters. For PIC simulations, it lies around 10%, that is, $v_{rec,PIC} \approx 0.1 v_A \approx 0.1c$, for magnetized collisionless plasmas (Sironi & Spitkovsky 2014; Werner et al. 2018; Guo et al. 2015), which are the typical conditions in the inner flow surrounding Sgr A*[1]. Resistive GRMHD simulations indicate a slower rate of about 1%, so that $v_{rec,MHD} \approx 0.01c$ (see the discussion in Ripperda et al. 2022), but this applies to collisional environments, which are less similar to the vicinity of Sgr A*.

Fresh plasma flows into the current sheet at the reconnection rate v_{rec} and is accelerated by the electric field generated in the current sheet, usually giving rise to power-law energy distributions of electrons (Sironi & Spitkovsky 2014; Werner et al. 2018). Inside the current sheet, the particles are trapped in the plasmoids, which act as particle reservoirs (Sironi & Spitkovsky 2014) that can merge in a macroscopic magnetic island, that is, a large plasmoid. In Ripperda et al. (2022), magnetic flux dissipation through reconnection lasts for $\sim 100 r_g/c \sim 30$ min, and the resulting hot spot orbits for $\sim 500 r_g/c \sim 150$ min before it disappears by losing its coherence through interaction with the surrounding flow.

In the global PIC simulation of El Mellah et al. (2022), the authors studied magnetic reconnection in the sheath of a relativistic jet, working with magnetic field loops that coupled the BH to the accretion disk. The resulting plasmoids evolve off-plane, propagate away from the BH, and easily merge with each other to form macroscopic plasmoids that radiate high amounts of energy in the form of nonthermal radiation. The underlying mechanism, first described by Uzdensky (2005) and de Gouveia dal Pino & Lazarian (2005), relies on the accretion of poloidal magnetic field loops onto a spinning BH. When the inner footpoint of the loop reaches the BH ergosphere, the magnetic field line experiences strong torques due to the frame dragging effect, while its other footpoint on the disk rotates at the local Keplerian speed. Thus, the toroidal component of the magnetic field quickly grows in the innermost regions, propagates upstream along the field line, and leads to the opening of the magnetic loop above a certain magnetic loop size. On the outermost closed magnetic field line (called the separatrix), a Y-point appears. Here, plasmoids form and flow away along an inclined current sheet above the disk (Fig. 5). In the PIC simulations of El Mellah et al. (2022), a cone-shaped reconnecting current sheet formed in which vivid particle acceleration takes place. Electrons and positrons pile up into outflowing plasmoids, where they cool through synchrotron radiation. This topological configuration, in which some magnetic field lines anchored in the

[1] It is likely that the accretion flow surrounding Sgr A* is in a magnetically arrested disk (MAD; see Narayan et al. 2003) regime, that is, it has strong poloidal magnetic fields in the inner regions (GRAVITY Collaboration 2018; Dexter et al. 2020b).

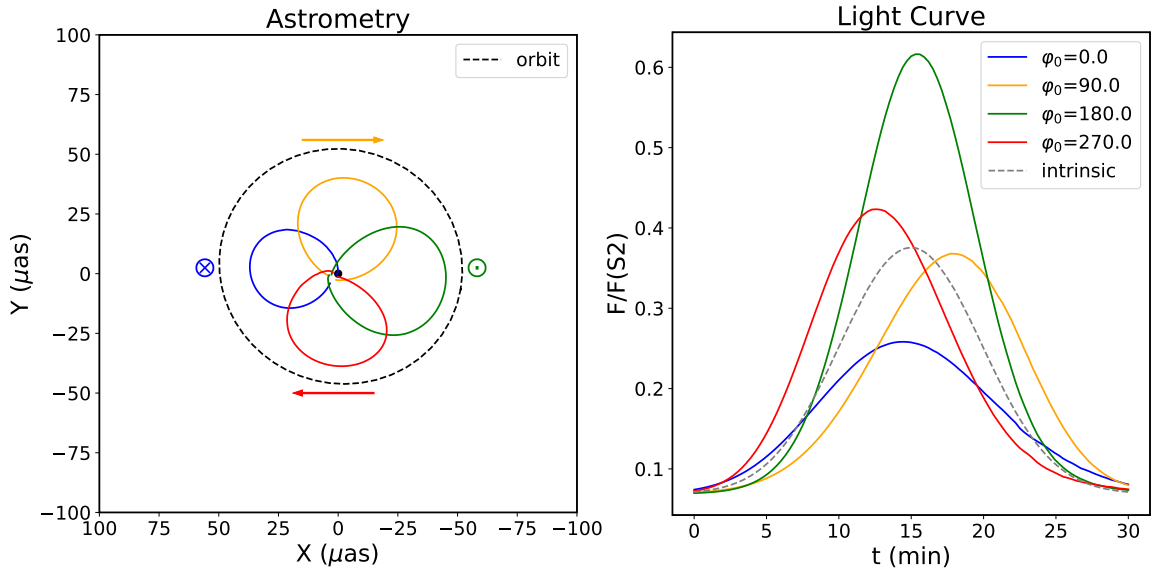

Fig. 4. Astrometry (left) and light curves (right) of the hot spot – jet model for four initial azimuthal angles φ_0 of 0 deg in blue, 90 deg in orange, 180 deg in green, and 270 deg in red. The dashed black line shows the primary image centroid track without a quiescent jet (clockwise). The jet dominates the beginning and end of the flares. The observed centroids thus start and end close to the jet centroid. The apparent orbits rotate around the latter with φ_0 as the maximum of emission occurs at different φ. The Gaussian modulation, which has a typical duration of $t_\sigma = 15$ min (dashed gray line; this is the same for the four the curves) is affected by relativistic effects. For negative X (right part of the astrometry), the beaming, combined with relativistic Doppler effect, amplifies the flux from the hot spot, and in the positive X (left part of the figure), the beaming decreases the flow. The black dot in the left panels represents the position of Sgr A*.

disk close within the event horizon is coherent with what is seen in resistive GRMHD simulations during the short episodes of flux repulsion that separate different accretion regimes. During approximately 100 rg/c, these simulations show an essentially force-free funnel surrounded by merging plasmoids that formed in the jet sheath and in the equatorial plane Ripperda et al. (2022), Chashkina et al. (2021).

3.1. Plasmoid model from magnetic reconnection

The aim of this section is to develop a semi-analytic large plasmoid model (which we call plasmoid model) that is inspired by the reconnection literature reviewed above. The interest in this model, compared to the latest GRMHD or GRPIC modeling is to remain as agnostic as possible regarding the physical conditions close to Sgr A*, encapsulate a large parameter space in a single model and perform simulations within a limited computing time, allowing to explore the large parameter space and to compare it to astrometric and photometric data. Our hope is that this model can be fed with the results of more elaborated simulations and also bring constraints to these simulations by determining the features of the modeling that are important in order to explain the data.

The main features of our model are illustrated in Fig. 5 and are inspired by the recent GRPIC results of El Mellah et al. (2022). We considered a single plasmoid, which was modeled as a sphere of hot plasma with a constant radius. This macroscopic plasmoid is understood as the end product of a sequence of microscopic plasmoid mergers. The spherical geometry was chosen only for simplicity because current data are certainly unable to make a difference between various geometries.

3.1.1. Plasmoid motion

We considered that the magnetic reconnection event occurs close to the black hole and that the resulting plasmoid is ejected along the jet sheath (Ripperda et al. 2020; El Mellah et al. 2022). Thus, we defined a conical motion (as in Ball et al. 2021), defined by a constant polar angle $\theta = \theta_0$ and the initial conditions r_0, θ_0, φ_0, v_{r0}, and $v_{\varphi 0}$. The subscript 0 reflects the initial value of a given parameter in Boyer–Lindquist coordinates. As in Ball et al. (2021), we set a constant radial velocity $v_r = v_{r0}$, and the azimuthal velocity was defined through the conservation of the Newtonian angular momentum,

$$v_\varphi(t) = v_{\varphi 0} \frac{r_0^2}{r(t)^2}. \tag{3}$$

The azimuthal angle was obtained by integrating Eq. (3),

$$\varphi(t) = \varphi_0 + r_0^2 \frac{v_{\varphi 0}}{v_r} \left(\frac{1}{r_0} - \frac{1}{r(t)} \right). \tag{4}$$

In the GRPIC simulations performed by El Mellah et al. (2022), the plasmoids are formed in the vicinity of the black hole at the Y-point and are ejected into the black hole magnetosphere. We therefore restrict our study to $v_r > 0$. An important feature of our model is the fact that the initial azimuthal velocity of the plasmoid is naturally super-Keplerian. The Y-point from which the plasmoid is generated is indeed anchored on the equatorial plane of the accretion flow through the separatrix field line. It will therefore typically rotate at the Keplerian speed corresponding to the footpoint of the line, that is, at a velocity higher than the Keplerian velocity corresponding to the initial cylindrical radius of the plasmoid.

3.1.2. Growth and cooling phases

We considered two phases in the lifetime of the plasmoid that aim at modeling the ascending and descending phases of the observed flare light curves. First the growth phase, which lasts a total time $t_{\rm growth}$, the plasmoid continuously receives freshly

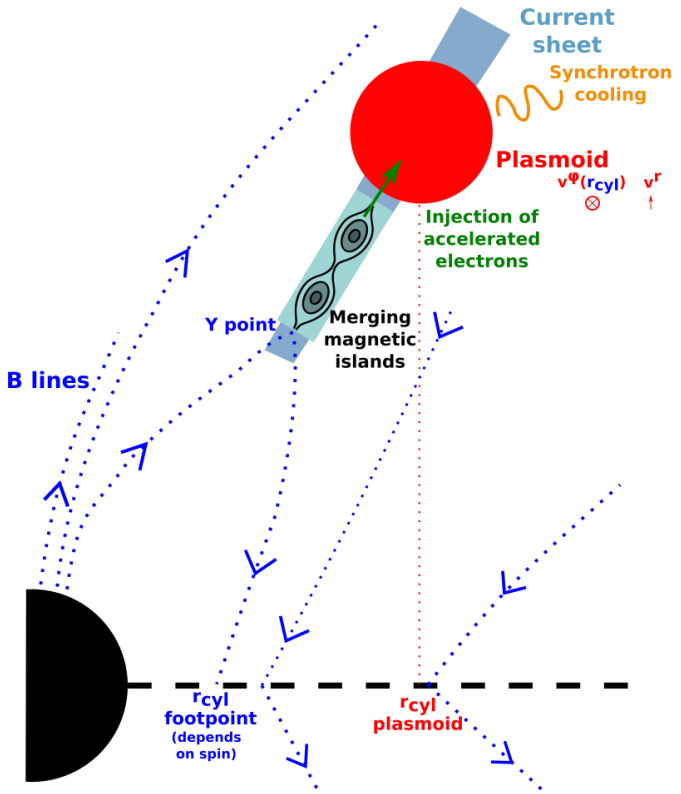

Fig. 5. Sketch of magnetic reconnection in the black hole magnetosphere as shown by El Mellah et al. (2022) on which our plasmoid model is built. Three types of magnetic field lines are shown: the lines threading the event horizon, which extends to infinity, the lines anchored on the disk, which also extends to infinity, and the separatrix, which links the disk and the black hole event horizon. The latter form a Y-point and a current sheet in which the plasmoid chains are formed. We model a single plasmoid as the result of multiple mergers.

accelerated particles at a constant rate resulting from the merging of microscopic plasmoids from reconnection into our large plasmoid. They mix with old electrons that are cooled by synchrotron radiation. The growth time $t_{\rm growth}$ corresponds to the lifetime of the reconnection engine, that is, the duration of magnetic flux dissipation. After $t = t_{\rm growth}$, the plasmoid enters the cooling phase. We assume that magnetic reconnection is quenched and plasmoids no longer merge, so that injection of fresh plasma stops and the plasmoid cools by emitting synchrotron radiation. We neglect particle escape and adiabatic losses.

The duration of the growth phase is set both by the reconnection rate and the speed at which magnetic flux is advected by the accretion flow into the current sheet. Parfrey et al. (2015) reported that the accretion of successive magnetic loops of opposite polarity activates this process. The typical transition duration is about $100r_{\rm g}/c$. This duration is representative of the dissipation of the magnetic flux of one magnetic loop that is set by both the size of the loop and the accretion speed, which the authors fixed to $2r_{\rm g}$ and $c/200$, and the reconnection rate, which was fixed by the prescribed resistivity. Resistive GRMHD simulations of magnetically arrested disks (Narayan et al. 2003) support these values (e.g., Ripperda et al. 2020), but do not reach realistically high reconnection rates (Bransgrove et al. 2021). In the more ab initio PIC simulations of El Mellah et al. (2022), the reconnection rate is more realistic (∼10%, Sironi & Spitkovsky 2014; Werner et al. 2018), but due to the high computational cost of the simulations, they did not work over a duration that was long enough to model the inward drift of the magnetic footpoints on the disk. As a consequence, the reconnection rate is accurate, but the fueling magnetic flux is artificially steady and acts as an infinite reservoir over the $\sim 200r_{\rm g}/c$ covered by the simulation. A coupling between GRMHD, force-free, and PIC simulations to jointly describe the disk, the corona, and the current sheet, respectively, is still missing. In this context, we considered a duration $t_{\rm growth}$ of the growth phase of about $100r_{\rm g}/c$, corresponding to a typical episode of magnetic flux dissipation set by the two rates at which magnetic flux is advected into the current sheet and dissipated by magnetic reconnection.

3.1.3. Evolution of the electron distribution

Next, we prescribe the emission and absorption mechanism in the plasmoid. Most studies use chosen electron distributions, with analytical prescriptions for their evolution at best. Ball et al. (2021) used a fixed thermal distribution with a linear increase in the number density for the rising part of the light curve and a decrease in the temperature following Eq. (D.7) for the cooling. Scepi et al. (2022) used a kappa distribution with an exponential cutoff and a synchrotron cooling break for the plasma emission generating X-ray flares. While their evolution of the plasma parameters (number density, temperature, and magnetic field) is more elaborate than in our model, their approximation is valid only while injection and cooling are balanced. When the injection stops, the shape of the electron distribution changes rapidly (see Fig. 6). We chose a different approach by evolving the electron distribution in the plasmoid by solving the kinetic equation

$$\frac{\partial N_{\rm e}(\gamma,t)}{\partial t} = \frac{\partial}{\partial \gamma}\left(-\dot{\gamma}_{\rm syn}\, N_{\rm e}(\gamma,t)\right) + Q_{\rm inj}(\gamma), \tag{5}$$

where γ is the Lorentz factor of the electrons, $Q_{\rm inj}$ is the injection rate, and $N_{\rm e} = {\rm d}n_{\rm e}/{\rm d}\gamma$ is the electron number density distribution, using the EMBLEM code (Dmytriiev et al. 2021). The term

$$-\dot{\gamma}_{\rm syn} N_{\rm e} = \frac{4\sigma_T U_B}{3m_{\rm e}c}(\gamma^2-1)N_{\rm e} \tag{6}$$

of the right-hand side describes the synchrotron cooling of the plasmoid particles, with $U_B = B^2/(8\pi)$. In our approach, we did not model the details of the magnetic reconnection process, but instead described the supply of freshly accelerated particles to the plasmoid by magnetic reconnection. Therefore, for the injection rate $Q_{\rm inj}(\gamma)$ in Eq. (5), we used the following expression, assuming a constant injection rate:

$$Q_{\rm inj}(\gamma) = \begin{cases} \dfrac{4\pi N_{\rm e}^{\kappa}(\gamma)}{t_{\rm growth}} & \text{in the growth phase,} \\ 0 & \text{in the cooling phase,} \end{cases} \tag{7}$$

where $N_{\rm e}^{\kappa}(\gamma)$ is the distribution of the injected particles, which follows the kappa distribution, that is, a thermal core with a power-law tail following

$$N_{\rm e}^{\kappa}(\gamma) = \frac{N}{4\pi}\gamma(\gamma^2-1)^{1/2}\left(1+\frac{\gamma-1}{\kappa\Theta_{\rm e}}\right)^{-(\kappa+1)}, \tag{8}$$

with a normalization factor $N = 1/2n_{\rm e}(\kappa-2)(\kappa-1)\kappa^{-2}\Theta_{\rm e}^{-3}$, where $n_{\rm e}$ and $\Theta_{\rm e}$ are the density and dimensionless temperature of the injected plasma. The index κ is defined as

$$\kappa = p + 1 = A_{\rm p} + B_{\rm p}\tanh\left(C_{\rm p}\,\beta_{\rm b}\right) + 1, \tag{9}$$

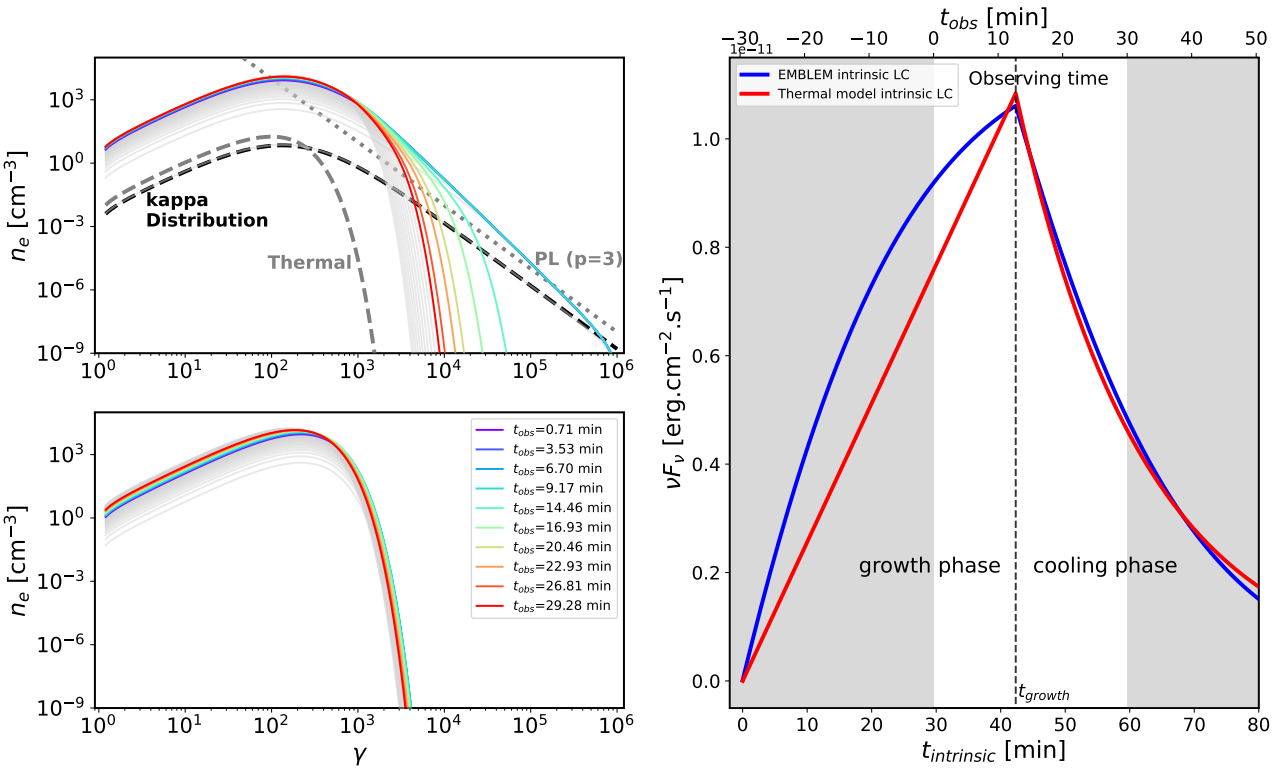

Fig. 6. Top left: evolution of the electron distribution in our model with EMBLEM at each observing time of the flare on 22 July 2018. The dotted black line corresponds to the injected κ electron distribution, which is composed of a thermal core with a power-law tail. The parameters are listed in Table 3. Bottom left: evolution of the electron distribution in the thermal model inspired by Ball et al. (2021) at each observing time of the flare on 22 July 2018. The parameters used for this distribution are the same as in our model (listed in Table 3), but with a dimensionless temperature of $\Theta_e = 109$ and a magnetic field of $B = 20$ G. Right: full intrinsic light curves of the two models. We plot the light curve from the beginning of the growth phase in this panel, and in the left panels, we plot the distribution at the observed time of Fig. 8 ($t_{obs} = t_{intrinsic} - 29.6$ min).

where

$$A_p = 1.8 + 0.7/\sqrt{\sigma_b}, B_p = 3.7\,\sigma_b^{-0.19}, C_p = 23.4\,\sigma_b^{0.26}, \quad (10)$$

following Ball et al. (2018), Werner et al. (2018), where p is the power-law index of the nonthermal part of the distribution, $\sigma_b \gg 1$ is the plasma magnetization of the accelerating site, and $\beta_b \ll 1$ is the ratio of proton thermal pressure to magnetic pressure of the accelerating site. If the magnetization at the accelerating site satisfies $\sigma_b \geq 100$ (Crinquand et al. 2021), then κ is in the range of $[2.8, 4.4]$ depending on β_b. This implies that the spectral index α ($\nu F_\nu \propto \nu^\alpha$) is between -0.5 and 0.5, which perfectly agrees with the measured indices for flares (Fig. 32 in Genzel et al. 2010). We note that realistic values for the magnetization in the funnel region of Sgr A* can be orders of magnitude higher than 100 (see Ripperda et al. 2022), which results in a smaller parameter space for κ that is closer to the low boundary.

The bounds of the electron Lorentz factor were chosen to satisfy $\gamma_{min} = 1$ and $\gamma_{max} = 10^6$ (Eq. (3) of Ripperda et al. 2022). When solving the kinetic Eq. (5), we assumed that the density of the plasmoid particles follows

$$n_e(t) = \begin{cases} n_e^{max} \times t/t_{growth} & \text{in the growth phase,} \\ n_e^{max} & \text{in the cooling phase.} \end{cases} \quad (11)$$

This high maximum Lorentz factor is needed to also power X-ray flares with synchrotron alone. However, Ripperda et al. (2022) suggested a lower maximum Lorentz factor $\gamma_{max} \sim 10^4$ in the plasmoid as electrons cool during their travel time between the acceleration site and the plasmoid. This lower value results in a marginally lower flux in the NIR because most of the emission at this wavelength comes from lower-energy electrons, which can be compensated for with a slightly higher maximum number density. The temperature of the injected particles remains fixed in the growth phase, and we defined a uniform and time-independent tangled magnetic field in the plasmoid. This is also a simplifying assumption, and we intend to consider the impact of the magnetic field geometry on the polarized observables in future work.

The EMBLEM code does not only solve for the evolution of the electron distribution, it also provides the associated synchrotron emission and absorption coefficients of the plasmoid particles. We can thus compute an image of our plasmoid scenario by backward-integrating null geodesics in the Schwarzschild space time from a distant observer screen, and integrate the radiative transfer equation through the plasmoid by reading the tabulated emission and absorption provided by EMBLEM. This step was performed by means of the GYOTO[2] ray-tracing code (see Appendix B for details; Vincent et al. 2011; Paumard et al. 2019). The input parameters that we used for the code are listed in Table 3. With these values of density and magnetic field strength, we obtain a magnetization inside the plasmoid of $\sigma_p \sim 10^{-2}$ from the end of the growth phase because neither the density nor the magnetic field evolve.

[2] https://gyoto.obspm.fr

Table 3. Input parameters of the EMBLEM code for the simulation of the electron distribution evolution.

Parameter	Symbol	Value
Plasmoid		
Magnetic field [G]	B_p	15
Plasmoid radius [r_g]	R_p	1
Minimal Lorentz factor	γ_{min}	1
Maximum Lorentz factor	γ_{max}	10^6
Kappa distribution index	κ	4.0
Kappa distribution temperature	Θ_e	50
Maximum electron number density [cm^{-3}]	$n_{e,max}$	5×10^6
Growth timescale [r_g/c]	t_{growth}	120

Notes. These parameters were used for the July 22 flare of GRAVITY Collaboration (2018).

Table 4. Orbital parameters of the plasmoid model following a conical motion used for the comparison of the flares on 22 July 2018 observed by GRAVITY Collaboration (2018).

Parameter	Symbol	July 22
Plasmoid		
Time in EMBLEM at zero observing time [min]	$t^{emblem}_{obs,0}$	29.6
Initial cylindrical radius [r_g]	$r_{cyl,0}$	10.6
Polar angle [deg]	θ	135
Initial azimuthal angle [deg]	φ_0	280
Initial radial velocity [c]	$v_{r,0}$	0.01
Initial azimuthal velocity [rad s^{-1}]	$v_{\varphi,0}$	0.042
X position of Sgr A* [μas]	x_0	0
Y position of Sgr A* [μas]	y_0	0
PALN [deg]	Ω	160

3.2. Importance of evolving the electron distribution

One of the most important aspects of our model is the self-consistent evolution of the electron distribution function and corresponding radiative transfer in the plasmoid. We illustrate the importance of taking the evolution of the electron distribution into account by comparing our model with another reconnection plasmoid model inspired by Ball et al. (2021). We show the evolution of the electron distribution in our plasmoid model for the parameters listed in Tables 3 and 4 in the top left panel of Fig. 6 (see Sect. 3.3 for details) and the associated spectral energy density (SED) in Fig. 7. During the growth phase ($t_{obs} < 10$ min), the distribution is stationary for $\gamma > 10^3$ as the injection is balanced by the cooling. After the end of the growth phase, the shape of the distribution changes rapidly as only cooling is left. We show the light curve obtained with our model in the right panel of Fig. 6 (in red) and with a model inspired by Ball et al. (2021), who did not take the nonthermal electrons into account, that is, who used a thermal distribution, with a linear increase in the number density with a fixed temperature during the growth phase and an analytical prescription for the temperature decrease during the cooling phase using Eq. (D.7) and assuming $\Theta_e = \gamma/3$. While this model gives a similar intrinsic light curve as our model, the required dimensionless temperature is twice as high as ours ($\Theta_e = 109$), with a magnetic field of $B = 20$ G to faster cool the lower-energy electrons. The evolution of the distribution with this model is shown in the bottom left panel of Fig. 6. We do not need a high temperature like this as most of the emission comes from high-energy electrons, which are nonthermal in our model, as suggested by PIC simulations (Rowan et al. 2017; Werner et al. 2018; Ball et al. 2018; Zhang et al. 2021). Our temperature could be even lower with a harder (i.e., lower) κ index. The cooling of the electron distribution through synchrotron radiation is difficult to model properly and needs a kinetic approach, as in our plasmoid model.

3.3. Comparing GRAVITY 2018 flare data with our plasmoid model

We wish to determine whether we can reproduce the general features of the observed light curve and astrometry of the flare on 22 July 2018 reported by GRAVITY Collaboration (2018) with our plasmoid model. We compare in Fig. 8 the flare on 22 July 2018 observed by GRAVITY (in black) and our plasmoid model (red line) with the parameters listed in Tables 3 and 4. For comparison, we show the intrinsic light curve (dashed line) obtained by removing all the relativistic effects (Doppler effect, beaming, and secondary image).

This comparison is not the result of a fit and was obtained by estimating the relevant parameters using simple physical arguments. The rise time and slope of the light curve are mainly monitored by (i) the growth time, (ii) our choice of linear evolution of the electron density (which enters the injection function), (iii) the relativistic beaming effect, and thus (iv) the initial azimuthal position of the plasmoid, φ_0, which has a strong impact on beaming, as illustrated in the right panel of Fig. 4. The decaying part of the light curve is monitored by the synchrotron cooling time, thus by the magnetic field strength, and by the beaming effect. The maximum of the light curve can be estimated by means of an analytical formula that we derive in Appendix C.2. This maximum mainly depends on the maximum number density $n_{e,max}$, but also on the temperature and κ index of the distribution. These parameters are degenerate and thus not constrained with the NIR flare data alone. Nevertheless, GRMHD (Dexter et al. 2020b; Ripperda et al. 2022; Scepi et al. 2022) and GRPIC simulations (El Mellah et al. 2022) of magnetic reconnection suggest that the density in the plasmoid is higher than that of its close environment in the current sheet, approximately the density at the base of the jet, close to the event horizon, but lower than in the disk. The two remaining parameters (Θ_e, κ) that describe the shape of the distribution are still fully degenerate, however. The initial position and velocity of the plasmoid have a strong impact on the astrometric trace on sky. We guessed the initial azimuthal velocity based on the following reasoning. The Keplerian velocity of the plasmoid at its initial cylindrical radius is $v_{Kep} \sim 0.31c$ (for our choice of initial cylindrical radius given in Table 4, $r_{cyl} = 10.6\,r_g$). However, as discussed in Sect. 3.1, our model naturally leads to a super-Keplerian initial velocity to the plasmoid. The initial azimuthal velocity of the plasmoid is that of the footpoint of the separatrix (see Fig. 5). Based on Fig. 8 of El Mellah et al. (2022), we can determine the radius of the footpoint, r_{fp}, of a separatrix giving rise to a Y point located at a cylindrical radius of $\approx 10\,r_g$. We find $r_{fp} = (4.7 \pm 0.5)\,r_g$, which translates into an orbital velocity $v_{\varphi,0}$ between $0.41c$ and $0.45c$. The upper bound of this interval compares well with the data of the July 22 flare. We note that this estimate of the initial azimuthal velocity is anchored in the model of El Mellah et al. (2022) and thus depends on their choice of initial condition, in particular, on the initial profile of their magnetic field.

We note that the fiducial values proposed in Tables 3 and 4 represent a set of parameters with values that are inspired by

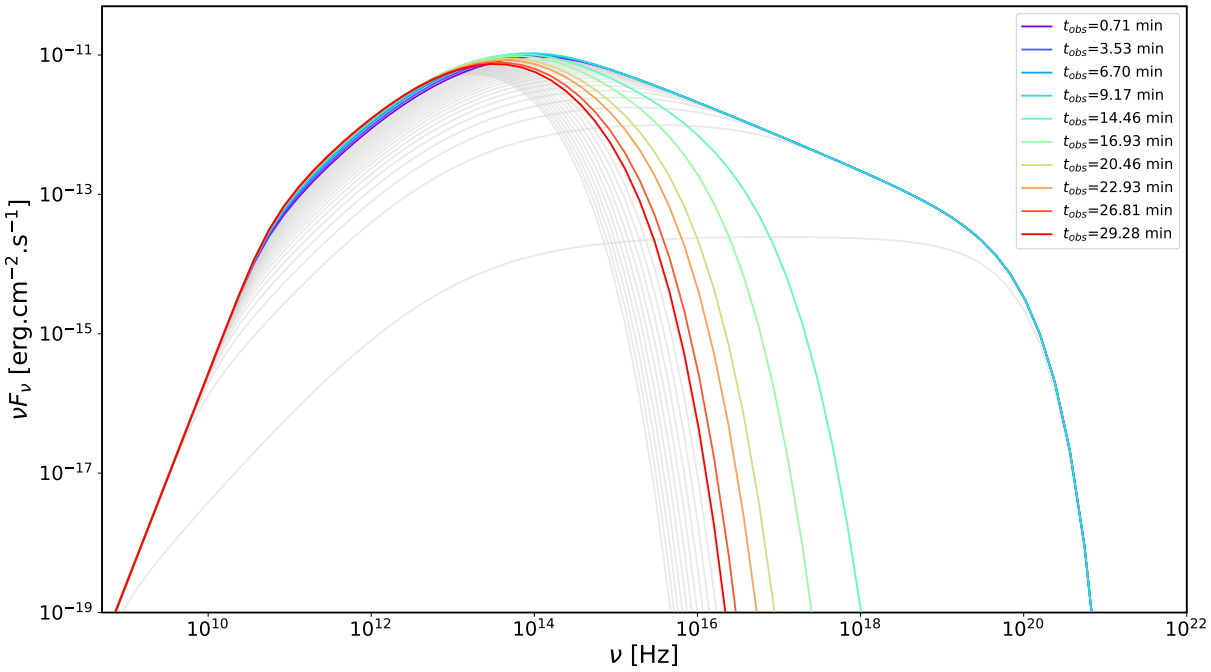

Fig. 7. Intrinsic SED evolution of our plasmoid model from radio to X-rays with the parameters listed in Table 3. The color code of the time is the same as in Fig. 6. Gray lines show the SED out of the observing time.

numerical simulations of reconnection that reproduce the key observational features of the data for the July 22 flare. This setup is not unique and is not the result of a fit. We reserve the exploration of the full parameters space (freeing some fixed or constrained parameters, e.g., maximum number density, growth time, and inclination) for a future work. Nevertheless, our model disfavors a short growth time ($t_{\rm growth} < 50 r_{\rm g}/c$) for this particular flare. Overall, our plasmoid model jointly describes the astrometry and the flux variation of the flare on 22 July 2018 measured by GRAVITY Collaboration (2018) for the first time, considering a model with a specific emission prescription. Magnetic reconnection is thus a viable scenario to explain the Sgr A* flares.

4. Limitations of our plasmoid model

Our plasmoid model is vastly simplified with respect to the complexity of realistic magnetic reconnection events in the environment of black holes. We review its main limitations below.

i. We considered a single plasmoid, while the instability of thin current sheets gives rise to a dynamic flow of merging magnetic islands. Our argument for this simplification is that the merging process is certainly highly dependent on the unknown initial conditions, and that the final larger and brighter product of the cascade is likely to dominate the observed signal.

ii. The initial condition for the plasmoid velocity was simply imposed for the radial motion and was based on a particular GRPIC model as regards the azimuthal motion.

iii. The evolution of the plasma parameters (density, temperature, and magnetic field) were chosen to be either constant or linear, which is highly simplified compared to a realistic scenario. However, we consider that these evolutions are very likely to be strongly dependent on the initial conditions of the flow, so that they are weakly constrained.

iv. The values of almost all the parameters except for mass and distance of Sgr A* are poorly constrained. We chose a set of values that are reasonable according to simulations. Future work is needed to investigate the details of the parameter space.

v. We modeled the plasmoid by a homogeneous sphere for simplicity from the circle plasmoid seen in 2D GRMHD (Nathanail et al. 2020; Ripperda et al. 2020; Porth et al. 2021) and PIC simulations (Rowan et al. 2017; Ball et al. 2018; Werner et al. 2018). The 3D aspect of this plasmoid is cylindrical (flux ropes) in the GRMHD (Bransgrove et al. 2021; Nathanail et al. 2022; Ripperda et al. 2022) and PIC (Nättilä & Beloborodov 2021; Zhang et al. 2021) simulations. Thus, a realistic geometry of the flare source is likely more complex than in our model. We note that the exact geometry of the flare is not relevant because we only track the centroid position because much of the flare source is not too extended, and we considered a tangled magnetic field. However, the coherence time of the structure might be shorter in 3D and might have an impact on the rise time of the light curve. Further 3D simulations studies are needed to better model the shape of the flux ropes and their evolution.

vi. We neglected any shearing of the plasmoid and considered that it remains identical to itself throughout the simulation. Differential rotation is likely to stretch the plasmoid over its orbit, however, and destroy its coherence (Hamaus et al. 2009; GRAVITY Collaboration 2020c).

vii. We considered a tangled magnetic field in the plasmoid and therefore did not consider the impact of the magnetic field geometry on the observable. The magnetic field geometry of the quiescent flow is likely to be ordered and vertical if Sgr A* is strongly magnetized. The magnetic field in the plasmoid, which is our interest here, could be either helical (plasmoids) or vertical for large flux tubes (Ripperda et al. 2022).

viii. During a flare, the quiescent state can change in a non-axisymmetrical way (Ripperda et al. 2022). This will push the centroid position of the quiescent farther away from the

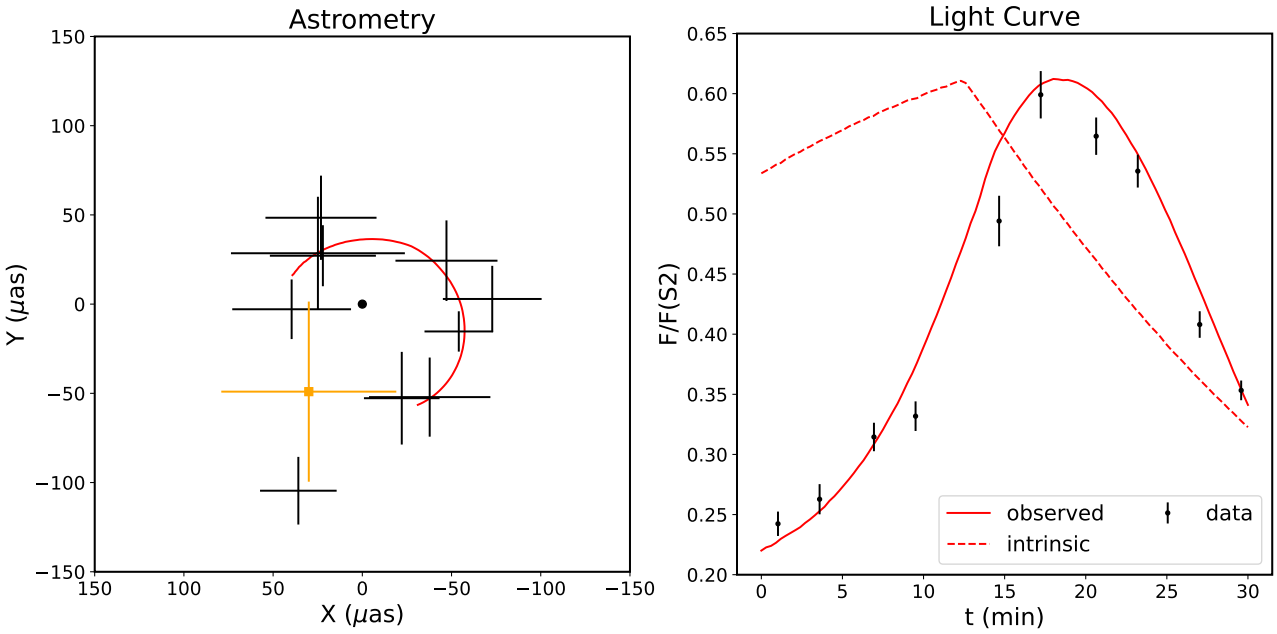

Fig. 8. Data and plasmoid models of the flares from July 22, 2018. The left panels shows the astrometry of the flare while the right panel shows the observed (full line) and intrinsic (dashed line) light curves. The parameters of the model are listed in Tables 3 and 4. Note that this is not the result of a fit. The black dot in the left panels represents the position of Sgr A* in GYOTO and the orange cross represent the position of Sgr A* measured through the orbit of S2.

location of the center of mass, which will affect the offset. We chose to use a static and axisymmetric quiescent model during the flare to avoid adding more degrees of freedom, which would lead to higher degeneracies and not to clearer constraints.

ix. We chose a high maximum Lorentz factor $\gamma_{\rm max} = 10^6$ to be able to power X-ray flares (but without any constraint for this study). However, high-energy photons lead to pair production and thus increase the number density in the plasmoid, which we did not take into account.

Despite these many limitations, we consider our model to be very interesting for fitting flare data because it allows covering a much broader set of physical scenarios than more elaborate simulations, which strongly depend on their assumptions regarding the relevant physics and the initial conditions.

5. Conclusion and perspectives

This paper is mainly focused on developing a new plasmoid model for Sgr A* flares, inspired by magnetic reconnection in black hole environments. Our semi-analytic model allowed us to study a broad parameter space within a reasonable computing time and is therefore well suited for data analysis. Our model considers nonthermal electrons accelerated by magnetic reconnection and injected into a spherical large plasmoid. We evolved the electron distribution through a kinetic equation taking synchrotron cooling and particle injection at a constant rate into account. We show in Appendix C.1 (Fig. C.3) the importance of taking the cooling of the electrons already in plasmoid during the growth phase into account. Our model also naturally accounts for a super-Keplerian velocity of the flare source through the dynamical coupling between the plasmoid and the inner regions of the accretion flow through magnetic field lines. One of the main results of this paper is that for the first time, we modeled the astrometry and light curve of the flares measured by GRAVITY Collaboration (2018) by explicit modeling of the emission zone.

Our conclusions regarding the three main points raised in the introduction are the following: (i) The marginally detected shift between the astrometric track of GRAVITY Collaboration (2018) and the center of mass might be due to the impact of the quiescent radiation of the background accretion flow. (ii) A dynamical coupling between the plasmoid and the inner accretion flow through closed magnetic field lines might naturally account for the super-Keplerian speed obtained by GRAVITY Collaboration (2018). (iii) In general, a large plasmoid due to magnetic reconnection in a thin current sheet in the black hole magnetosphere is a reasonable model to account for the main features of the GRAVITY Collaboration (2018) observables.

Section 3.3 showed that the temperature, density, and κ parameters of the plasmoid are degenerate. This degeneracy might be removed by simultaneous observations of NIR and X-ray flares. Moreover, synchrotron cooling leads to a translation of the electrons from the NIR-emitting band into the millimeter-emitting band, which could explain the submillimeter flare and its time lag with respect to the NIR. We therefore intend to consider the multiwavelength properties of our plasmoid model in future work, in order to better assess whether it can account for the complete flare data set of Sgr A*. A crucial recent observable of Sgr A* flares are the polarization QU loops (GRAVITY Collaboration 2018, 2020d; Wielgus et al. 2022b). We also intend to study the polarized properties of our plasmoid model and compare it to these recent constraints.

Acknowledgements. NA and FHV are very grateful to B. Cerutti, B. Crinquand, S. von Fellenberg, S. Gillessen, S. Masson, B. Ripperda, N. Scepi, and M. Wielgus for fruitful discussions. This work was granted access to the HPC resources of MesoPSL financed by the Region Ile de France and the project Equip@Meso (reference ANR-10-EQPX-29-01) of the programme Investissements d'Avenir supervised by the Agence Nationale pour la Recherche.

References

Backer, D. C. 1978, ApJ, 222, L9
Baganoff, F. K., Bautz, M. W., Brandt, W. N., et al. 2001, Nature, 413, 45
Ball, D., Sironi, L., & Özel, F. 2018, ApJ, 862, 80
Ball, D., Özel, F., Christian, P., Chan, C.-K., & Psaltis, D. 2021, ApJ, 917, 8
Barrière, N. M., Tomsick, J. A., Baganoff, F. K., et al. 2014, ApJ, 786, 46
Bower, G. C., Goss, W. M., Falcke, H., Backer, D. C., & Lithwick, Y. 2006, ApJ, 648, L127
Bower, G. C., Markoff, S., Dexter, J., et al. 2015, ApJ, 802, 69
Bower, G. C., Dexter, J., Asada, K., et al. 2019, ApJ, 881, L2
Bransgrove, A., Ripperda, B., & Philippov, A. 2021, Phys. Rev. Lett., 127, 055101
Brinkerink, C. D., Falcke, H., Law, C. J., et al. 2015, A&A, 576, A41
Broderick, A. E., & Loeb, A. 2006, MNRAS, 367, 905
Chashkina, A., Bromberg, O., & Levinson, A. 2021, MNRAS, 508, 1241
Chiaberge, M., & Ghisellini, G. 1999, MNRAS, 306, 551
Crinquand, B., Cerutti, B., Dubus, G., Parfrey, K., & Philippov, A. 2021, A&A, 650, A163
Crinquand, B., Cerutti, B., Dubus, G., Parfrey, K., & Philippov, A. 2022, Phys. Rev. Lett., 129, 205101
Davelaar, J., Mościbrodzka, M., Bronzwaer, T., & Falcke, H. 2018, A&A, 612, A34
de Gouveia dal Pino, E. M., & Lazarian, A. 2005, A&A, 441, 845
Dermer, C. D., & Schlickeiser, R. 2002, ApJ, 575, 667
Dexter, J., Jiménez-Rosales, A., Ressler, S. M., et al. 2020a, MNRAS, 494, 4168
Dexter, J., Tchekhovskoy, A., Jiménez-Rosales, A., et al. 2020b, MNRAS, 497, 4999
Dmytriiev, A., Sol, H., & Zech, A. 2021, MNRAS, 505, 2712
Do, T., Ghez, A. M., Morris, M. R., et al. 2009, ApJ, 691, 1021
Do, T., Witzel, G., Gautam, A. K., et al. 2019, ApJ, 882, L27
Dodds-Eden, K., Porquet, D., Trap, G., et al. 2009, ApJ, 698, 676
Dodds-Eden, K., Gillessen, S., Fritz, T. K., et al. 2011, ApJ, 728, 37
Eckart, A., Schödel, R., García-Marín, M., et al. 2008, A&A, 492, 337
Eckart, A., Baganoff, F. K., Morris, M. R., et al. 2009, A&A, 500, 935
Eisenhauer, F., Perrin, G., Rabien, S., et al. 2008, in The Power of Optical/IR Interferometry: Recent Scientific Results and 2nd Generation, eds. A. Richichi, F. Delplancke, F. Paresce, & A. Chelli, 431
Eisenhauer, F., Perrin, G., Brandner, W., et al. 2011, The Messenger, 143, 16
El Mellah, I., Cerutti, B., Crinquand, B., & Parfrey, K. 2022, A&A, 663, A169
Event Horizon Telescope Collaboration (Akiyama, K., et al.) 2022a, ApJ, 930, L12
Event Horizon Telescope Collaboration (Akiyama, K., et al.) 2022b, ApJ, 930, L16
Falcke, H. 1999, in The Central Parsecs of the Galaxy, eds. H. Falcke, A. Cotera, W. J. Duschl, F. Melia, & M. J. Rieke, ASP Conf. Ser., 186, 113
Fazio, G. G., Hora, J. L., Witzel, G., et al. 2018, ApJ, 864, 58
Genzel, R., Schödel, R., Ott, T., et al. 2003, Nature, 425, 934
Genzel, R., Eisenhauer, F., & Gillessen, S. 2010, Rev. Mod. Phys., 82, 3121
Ghez, A. M., Wright, S. A., Matthews, K., et al. 2004, ApJ, 601, L159
GRAVITY Collaboration (Abuter, R., et al.) 2017, A&A, 602, A94
GRAVITY Collaboration (Abuter, R., et al.) 2018, A&A, 618, L10
GRAVITY Collaboration (Abuter, R., et al.) 2020a, A&A, 638, A2
GRAVITY Collaboration (Abuter, R., et al.) 2020b, A&A, 636, L5
GRAVITY Collaboration (Bauböck, M., et al.) 2020c, A&A, 635, A143
GRAVITY Collaboration (Jiménez-Rosales, A., et al.) 2020d, A&A, 643, A56
GRAVITY Collaboration (Abuter, R., et al.) 2022, A&A, 657, L12
Guo, F., Liu, Y.-H., Daughton, W., & Li, H. 2015, ApJ, 806, 167
Hamaus, N., Paumard, T., Müller, T., et al. 2009, ApJ, 692, 902
Hora, J. L., Witzel, G., Ashby, M. L. N., et al. 2014, ApJ, 793, 120
Hornstein, S. D., Matthews, K., Ghez, A. M., et al. 2007, ApJ, 667, 900
Komissarov, S. S. 2004, MNRAS, 350, 427
Komissarov, S. S. 2005, MNRAS, 359, 801
Komissarov, S. S., & McKinney, J. C. 2007, MNRAS, 377, L49
Krichbaum, T. P., Graham, D. A., Witzel, A., et al. 1998, A&A, 335, L106
Liu, H. B., Wright, M. C. H., Zhao, J.-H., et al. 2016, A&A, 593, A44
Lo, K. Y., Schilizzi, R. T., Cohen, M. H., & Ross, H. N. 1975, ApJ, 202, L63
Loureiro, N. F., Schekochihin, A. A., & Cowley, S. C. 2007, Phys. Plasmas, 14, 100703P
Macquart, J.-P., Bower, G. C., Wright, M. C. H., Backer, D. C., & Falcke, H. 2006, ApJ, 646, L111
Marrone, D. P., Moran, J. M., Zhao, J.-H., & Rao, R. 2006, J. Phys. Conf. Ser., 54, 354
Marrone, D. P., Baganoff, F. K., Morris, M. R., et al. 2008, ApJ, 682, 373
Mauerhan, J. C., Morris, M., Walter, F., & Baganoff, F. K. 2005, ApJ, 623, L25
Michail, J. M., Wardle, M., Yusef-Zadeh, F., & Kunneriath, D. 2021a, ApJ, 923, 54
Michail, J. M., Yusef-Zadeh, F., & Wardle, M. 2021b, MNRAS, 505, 3616
Mościbrodzka, M., & Falcke, H. 2013, A&A, 559, L3
Narayan, R., Igumenshchev, I. V., & Abramowicz, M. A. 2003, PASJ, 55, L69
Nathanail, A., Fromm, C. M., Porth, O., et al. 2020, MNRAS, 495, 1549
Nathanail, A., Mpisketzis, V., Porth, O., Fromm, C. M., & Rezzolla, L. 2022, MNRAS, 513, 4267
Nättilä, J., & Beloborodov, A. M. 2021, ApJ, 921, 87
Nayakshin, S., Cuadra, J., & Sunyaev, R. 2004, A&A, 413, 173
Neilsen, J., Nowak, M. A., Gammie, C., et al. 2013, ApJ, 774, 42
Nowak, M. A., Neilsen, J., Markoff, S. B., et al. 2012, ApJ, 759, 95
Pandya, A., Zhang, Z., Chandra, M., & Gammie, C. F. 2016, ApJ, 822, 34
Parfrey, K., Giannios, D., & Beloborodov, A. M. 2015, MNRAS, 446, L61
Parfrey, K., Philippov, A., & Cerutti, B. 2019, Phys. Rev. Lett., 122, 035101
Paumard, T., Perrin, G., Eckart, A., et al. 2008, in The Power of Optical/IR Interferometry: Recent Scientific Results and 2nd Generation, eds. A. Richichi, F. Delplancke, F. Paresce, & A. Chelli, 313
Paumard, T., Vincent, F. H., Straub, O., & Lamy, F. 2019, https://doi.org/10.5281/zenodo.2547541
Ponti, G., De Marco, B., Morris, M. R., et al. 2015, MNRAS, 454, 1525
Porth, O., Chatterjee, K., Narayan, R., et al. 2019, ApJS, 243, 26
Porth, O., Mizuno, Y., Younsi, Z., & Fromm, C. M. 2021, MNRAS, 502, 2023
Ressler, S. M., Tchekhovskoy, A., Quataert, E., & Gammie, C. F. 2017, MNRAS, 467, 3604
Ripperda, B., Bacchini, F., & Philippov, A. A. 2020, ApJ, 900, 100
Ripperda, B., Liska, M., Chatterjee, K., et al. 2022, ApJ, 924, L32
Rowan, M. E., Sironi, L., & Narayan, R. 2017, ApJ, 850, 29
Rybicki, G. B., & Lightman, A. P. 1979, Radiative Processes in Astrophysics (New York: Wiley)
Rybicki, G. B., & Lightman, A. P. 1986, Radiative Processes in Astrophysics (New York: Wiley)
Scepi, N., Dexter, J., & Begelman, M. C. 2022, MNRAS, 511, 3536
Sironi, L., & Spitkovsky, A. 2014, ApJ, 783, L21
Tagger, M., & Melia, F. 2006, ApJ, 636, L33
Uzdensky, D. A. 2005, ApJ, 620, 889
Vincent, F. H., Paumard, T., Gourgoulhon, E., & Perrin, G. 2011, Class. Quant. Grav., 28, 225011
Vincent, F. H., Paumard, T., Perrin, G., et al. 2014, MNRAS, 441, 3477
Vincent, F. H., Abramowicz, M. A., Zdziarski, A. A., et al. 2019, A&A, 624, A52
von Fellenberg, S. D., Gillessen, S., Graciá-Carpio, J., et al. 2018, ApJ, 862, 129
Werner, G. R., Uzdensky, D. A., Begelman, M. C., Cerutti, B., & Nalewajko, K. 2018, MNRAS, 473, 4840
Wielgus, M., Marchili, N., Martí-Vidal, I., et al. 2022a, ApJ, 930, L19
Wielgus, M., Moscibrodzka, M., Vos, J., et al. 2022b, A&A, 665, L6
Witzel, G., Martinez, G., Hora, J., et al. 2018, ApJ, 863, 15
Witzel, G., Martinez, G., Willner, S. P., et al. 2021, ApJ, 917, 73
Yusef-Zadeh, F., Roberts, D., Wardle, M., Heinke, C. O., & Bower, G. C. 2006, ApJ, 650, 189
Zhang, H., Sironi, L., & Giannios, D. 2021, ApJ, 922, 261

Appendix A: Torus-jet model for the quiescent state

We used the torus-jet model of Vincent et al. (2019). Their jet model is restricted to an emitting sheath with an empty funnel, in agreement with GRMHD simulations (e.g., Mościbrodzka & Falcke 2013; Ressler et al. 2017; Davelaar et al. 2018; Porth et al. 2019). In their model, Vincent et al. (2019) define an opening and closing angle θ_1 and θ_2 , respectively, and a base height z_b to define the geometry of the jet. The number density and the temperature are defined by their values at the base height of the jet (n_e^J and T_e^J , respectively) and their profiles along the jet. The profile of the number density is fixed ($\propto r_{cyl}^{-2}$ with r_{cyl} the projected radius in the equatorial plane) and the temperature profile is set by the temperatures slope s_T ($\propto z^{-s_T}$ with z the height along the vertical, i.e. spin, axis). The jet emits synchrotron radiation from a κ electron distribution. The torus is defined by its central density and temperature (n_e^T and T_e^T , respectively). The profiles of these two quantities in the torus are governed by the polytropic index k and its geometry. The latter is defined by the inner radius r_{in} and the angular momentum l, but also on the metric (see Vincent et al. (2019) for more details). In contrast to the jet, we considered that the electron distribution of the torus is purely thermal.

We used the same algorithm as in Vincent et al. (2019) after correcting for a small technical issue leading to an overestimation of the number density and temperature. However, we changed the choice of the magnetization parameter in the jet sheath. As illustrated by Porth et al. (2019), for example, the jet sheath, which corresponds to the dominating emission region of the jet, coincides with the transition between the highly magnetized ($\sigma \gg 1$) funnel and the less magnetized ($\sigma \ll 1$) main disk body. Consequently, we fixed the magnetization to $\sigma = 1$ in the emitting jet sheath, while Vincent et al. (2019) used a low magnetization both in the jet and in the torus. Our choice leads to a lower density in the jet sheath than in Vincent et al. (2019). We found a best fit with a $\chi^2_{red} = 0.91$ using the same data points as Vincent et al. (2019). The values are reported in Table 1, and Fig. 2 shows the associated spectrum and the image at 2.2 μm. We obtain a magnetic field strength of 257 G for the jet and 212 G at the center of the torus. These values are higher than those in Bower et al. (2019), who considered a full thermal electron population with a higher temperature, but the values are on the same order as those in Scepi et al. (2022).

Appendix B: Ray-tracing setup

We considered a Kerr black hole with dimensionless spin parameter $a = 0$, described in Boyer-Lindquist (t, r, θ, φ) coordinates. We worked in units in which the gravitational constant and the speed of light were equal to 1, $G = c = 1$. Radii are thus expressed in units of the black hole mass M. We used the backward ray-tracing code `GYOTO`[3] (Vincent et al. 2011; Paumard et al. 2019) to compute images of our models at different epochs. Each pixel of our image corresponds to a direction on sky. For each pixel of the image (i.e., each direction), a null geodesic was integrated backward in time from the observer toward the black hole, integrating along this path the radiative transfer equation

$$\frac{dI_\nu}{ds} = -\alpha_\nu I_\nu + j_\nu \tag{B.1}$$

using the synchrotron emissivity j_ν and absorptivity α_ν coefficients, considering various electron distribution functions. This allowed us to determine the flux centroid for each epoch and trace its motion. In addition to astrometry, we also determined the total flux emitted as the sum of the intensity weighted by the element of solid angle subtended by each pixel for each epoch, which allowed us to plot the light curve. The images produced are 1000x1000 pixels with a field of view of 300 μas vertically and horizontally, which results in a resolution $< 0.1\ \mu as^2$/pixel. This high resolution is needed to properly resolve the secondary image, which has a very important role in both astrometry and light curve (see Sect. 2).

We modeled the quiescent state of Sgr A* at 2.2 μm with a jet (see Sect. 2.1). However, computing an image of the jet takes $\sim$ 200 times longer than an image of the flare source (i.e., the hot spot or the plasmoid, Sect. 2 and 3, respectively) because the jet is much more extended, and integrating the radiative transfer equation therefore takes much longer. The absorption in the jet is negligible, thus the flux emitted by the flare that crosses the jet is fully transmitted. We computed a single image of the jet that we added to each images of the hot spot a posteriori. We then calculated the total flux by summing the jet flux with the flux of the flare at a given time. The final centroid position was calculated by a simple barycenter of the two centroids (jet and flare).

Appendix C: Intrinsic emission of the plasmoid

C.1. Tests of the kinetic simulations

In our model, we followed the evolution of the electron distribution taking the injection of accelerated electrons by the merging of small plasmoids into our large plasmoid and their cooling through synchrotron radiation into account. The emissivity j_ν and absorptivity α_ν coefficients, needed to integrate the radiative transfer Eq. B.1, were computed through the formula of Chiaberge & Ghisellini (1999) and Rybicki & Lightman (1986) (with our notation)

$$j_\nu(t) = \frac{1}{4\pi}\int_{\gamma_{min}}^{\gamma_{max}} d\gamma N_e(\gamma, t) P_s(\nu, \gamma), \tag{C.1}$$

$$\alpha_\nu(t) = -\frac{1}{8\pi m_e \nu^2}\int_{\gamma_{min}}^{\gamma_{max}} \frac{N_e(\gamma, t)}{\gamma l}\frac{d}{d\gamma}[\gamma l P_s(\nu, \gamma)] \tag{C.2}$$

with

$$P_s(\nu, \gamma) = \frac{3\sqrt{3}}{\pi}\frac{\sigma_T c U_B}{\nu_B} x^2 \left\{K_{4/3}(x)K_{1/3}(x) - \frac{3}{5}x[K^2_{4/3}(x) - K^2_{1/3}(x)]\right\}, \tag{C.3}$$

where $l = (\gamma^2 - 1)^{1/2}$ is the electron momentum in units of $m_e c$, $x = \nu/(3\gamma^2\nu_B)$, $\nu_B = eB/(2\pi m_e c)$, and $K_a(t)$ is the modified Bessel function of order a. We note that Eq. C.3 is already averaged over the pitch angle. For standard distributions such as thermal, power-law, and κ distributions, these formulae are equivalent to the fits of Pandya et al. (2016) (see Appendix D) that we used to compute the quiescent synchrotron flux.

Because electrons start to cool as soon as they are injected into the plasmoid, the full distribution no longer is a κ distribution. However, turning the cooling off during the growth phase allows us to compare the results of `EMBLEM` to the fitting formulae of Pandya et al. (2016). As we inject electrons following their definition of the κ distribution with a linear increase

[3] https://gyoto.obspm.fr

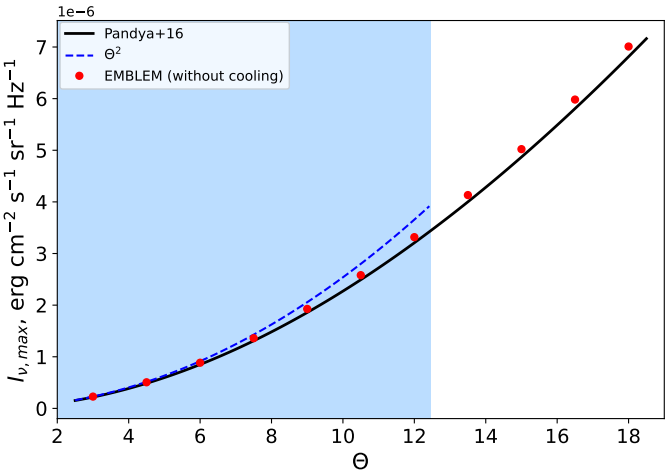

Fig. C.1. Specific intensity at the end of the growth phase ($t = t_{\rm growth} = 75\ r_{\rm g}/c$) of a κ distribution with $n_{\rm e} = 5 \times 10^6$ cm^{-3}, $B = 10$ G, and $\kappa = 4$ for a range of $\Theta_{\rm e}$ computed from the full fitting formulae of Pandya et al. (2016) (black curve) with the EMBLEM code (red dots) and with the high-frequency limit analytical expression (dashed blue curve). We overplot in light blue the range of $\Theta_{\rm e}$ in which $X_\kappa > 2000$, i.e., where the relative error between the high-frequency limit and the full formula is lower than 20%.

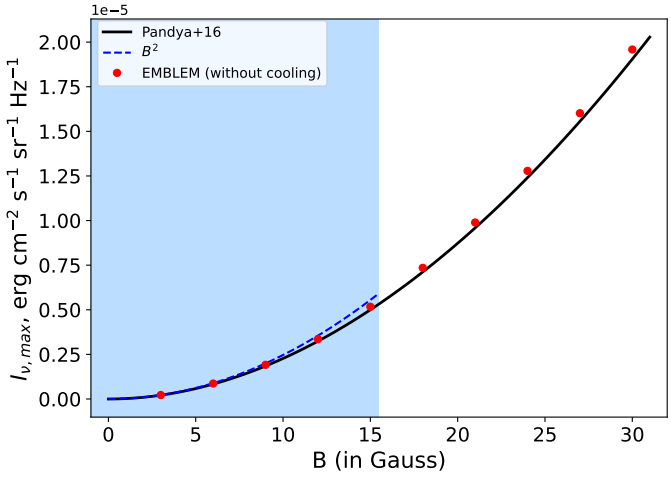

Fig. C.2. Same as in Fig.C.1 for a range of B and with $\Theta_{\rm e} = 10$.

in the number density, the two approaches show similar results (see Appendix D). In our cases, the absorption is very low, thus we neglect the absorption in these tests. We derived an analytical formula for the specific intensity from the high-frequency limit emissivity, Eq. D.3, depending on the number density $n_{\rm e}$, the electron temperature $\Theta_{\rm e}$, and the magnetic field B when the cooling is switched off during growth. We find in the case without cooling that keeping κ constant,

$$I_{\nu,max} \propto n_{e,max}\ \Theta^{\,\kappa-2}\ B^{\,\kappa/2},\ \text{if } X_\kappa > 2000. \tag{C.4}$$

We show the relative error of the maximum specific intensity between the EMBLEM code (red dots) and the formulae of Pandya et al. (2016) (black curve) depending on the electron temperature and the magnetic field in Figs. C.1 and C.2. We fixed the others parameters to $n_{\rm e} = 5 \times 10^6$ cm^{-3}, $\kappa = 4$, and $t_{\rm growth} = 75\ r_{\rm g}/c$. The values of EMBLEM agree well with the previous analytical expression (Eq. C.4) for low values of $\Theta_{\rm e}$ and B. For high values, we are beyond the validity of our approximations (in the intermediate-frequency regime of the fitting formula; see Appendix D). A comparison of the results of EMBLEM (without cooling) with the full fitting formula of Pandya et al. (2016) (black curves) results in an error lower than 5%, showing the good agreement between the two approaches.

C.2. Analytical estimate of the intrinsic light curve

Next, we computed the light curve emitted by the plasmoid that is affected by the relativistic effects. To reproduce a given light curve, we estimated the values of the parameters through characteristic scales. The growth time, which is a free parameter of the model, was estimated from the light curve, taking the beaming effect into account. It therefore depends on the orbital parameters. The synchrotron cooling time of an electron with Lorentz factor γ in a magnetic field B reads

$$t_{cool} = \frac{3}{4}\frac{m_{\rm e}c}{\sigma_T U_B \gamma}, \tag{C.5}$$

with σ_T the electron Thomson cross section and U_B the magnetic energy density. In a Dirac spectrum approximation, the Lorentz factor of an electron emitting an IR photon at 2.2 μm is (Rybicki & Lightman 1979)

$$\bar{\gamma} = \left(\frac{\nu m_{\rm e} c}{\eta e B}\right)^{1/2}, \tag{C.6}$$

with $\eta = (0.29 \times 3)/(2\pi)$ a dimensionless numerical factor (see Appendix E.2). We therefore constrained the magnetic field from the synchrotron cooling time as

$$t_{cool} = 19 \times \left(\frac{B}{20G}\right)^{-1.5} \left(\frac{\lambda}{2.2\mu m}\right)^{0.5} \text{min}. \tag{C.7}$$

When the cooling of the electrons during the growth phase is taken into account, we derive a lower flux than what we estimated from Eq. C.4. Because electrons start to cool directly after being injected, the integral of the distribution in Eq. C.1 and so the emissivity will always be lower than without cooling. The key parameter of synchrotron cooling is the cooling timescale (Eq. C.5), which depends on the magnetic field strength and on the initial energy of the electrons. It has to be compared to the growth time. With a low growth time, only high-energy electrons have the time to cool. A longer growth time allows lower-energy electrons to cool and so decreases the maximum flux of the light curve even more. With some approximations (see Appendix E for the details), we estimated the flux with cooling at $t = t_{\rm growth,}$

$$\nu F_\nu^{\rm syn}(\nu, t) = \frac{n_{\rm e} R_b^3\, \bar{\gamma} m_{\rm e} c^2}{12 D^2 t_{\rm growth}\, \kappa\theta^2} \begin{cases} \left[\Psi(\bar{\gamma}) - \Psi(\xi(\bar{\gamma}, t))\right], & \text{for } \nu < \tilde{\nu}(t) \\ \Psi(\bar{\gamma}), & \text{for } \nu \geq \tilde{\nu}(t) \end{cases}, \tag{C.8}$$

where $\tilde{\nu}(t) = (\eta e B)/(m_{\rm e} c b_c^2 t^2)$ is the frequency corresponding to the condition $\bar{\gamma} = 1/(b_c t)$ and

$$\Psi(x) = \left(1 + \frac{x-1}{\kappa\theta}\right)^{-\kappa} \left[x^2(\kappa - 1) + 2x(\kappa\theta - 1) + 2\theta(\kappa\theta - 2)\right]. \tag{C.9}$$

We plot the maximum light curve evolution relative to the magnetic field with EMBLEM with (blue crosses) and without (red crosses) cooling during the growth phase and the previous analytical expression in Fig. C.3 (black line). As expected, the

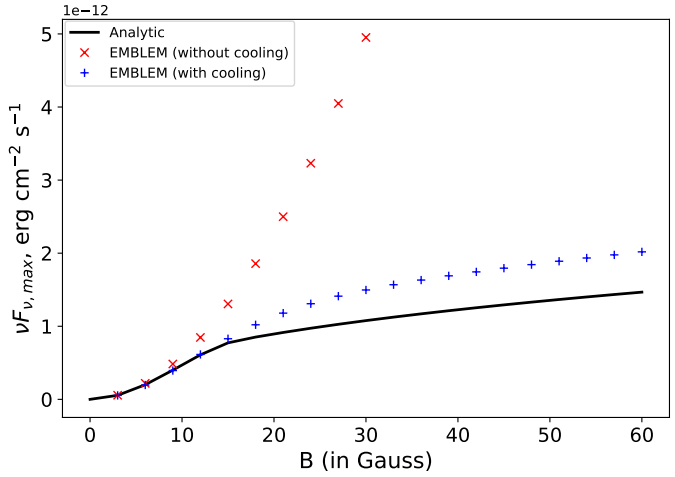

Fig. C.3. Evolution of the maximum flux $\nu F_\nu(t_{\rm growth})$ (at the end of the growth phase $t_{\rm growth} = 75\ r_g/c$) as a function of the magnetic field. We show the results of EMBLEM without cooling (red crosses) as in Fig. C.2. Allowing the cooling during the growth phase results in a lower maximum flux (blue crosses). The maximum flux with cooling can be estimated through Eq. C.8 (black line) which is divided in two regimes, the equilibrium regime where the magnetic field is strong enough to compensate the injection and creates a stationary state ($B \geq 16.2$ G) and nonstationary regime where not all electrons has cooled at $t_{\rm growth}$ ($B < 16.2$ G). The relative error between the analytical formula and the results of EMBLEM (with cooling) is below 30% in the whole domain and below 7% in the nonstationary regime.

cooling becomes more significant with a strong magnetic field until the maximum flux starts to decrease for very high values ($B > 100$ G). The two regimes of Eq. C.8 are clearly visible in Fig. C.3, with a turning point at $B = 16.2$ G. The maximum relative error of this approximation is lower than 30% compared to the results of EMBLEM in the stationary regime and lower than 7% for the nonstationary regime. This makes it a good approximation to estimate the peak light-curve flux.

Appendix D: Computing the synchrotron coefficients for the plasmoid

D.1. Fitting formulae of Pandya et al. (2016)

In the hot-spot model and for the test of EMBLEM, we used the fitting formula of Pandya et al. (2016) to compute the emissivity j_ν and absorptivity α_ν considering a well-defined κ distribution. This distribution has two regimes, the low- and high-frequency regimes. In the low-frequency limit, the emissivity is

$$j_{\nu,low} = \frac{n_e e^2 \nu_B}{c} X_\kappa^{1/3}\, sin(\theta)\, \frac{4\pi\Gamma(\kappa - 4/3)}{3^{7/3}\Gamma(\kappa - 2)} \tag{D.1}$$

and the absorption coefficient is

$$\alpha_{\nu,low} = \frac{n_e e^2}{\nu m_e c} X_\kappa^{-2/3} 3^{1/6} \frac{10}{41} \frac{2\pi}{(\Theta_e\,\kappa)^{10/3-\kappa}} \frac{(\kappa-2)(\kappa-1)\kappa}{3\kappa - 1} \times \Gamma\left(\frac{5}{3}\right)_2 F_1\left(\kappa - \frac{1}{3}, \kappa + 1, \kappa + \frac{2}{3}, -\Theta_e\,\kappa\right) \tag{D.2}$$

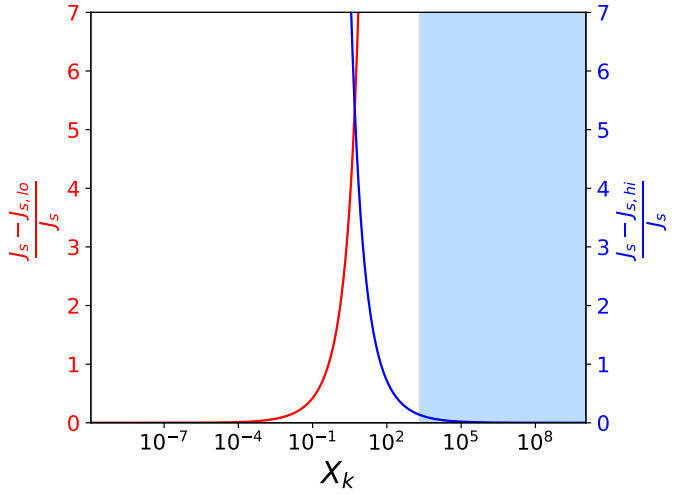

Fig. D.1. Relative error between the low-frequency regime (in red) and the high-frequency regime (in blue) fit formulae $J_{s,lo}$ ($J_{s,hi}$) of Pandya et al. (2016) and the full fit formula of the emission coefficient J_s as a function of $X_\kappa = \frac{\nu}{\nu_\kappa}$ with $\nu_\kappa = \nu_B\,(\Theta_e\kappa)^2$.

where ${}_2F_1$ is the hypergeometric function. In the high-frequency limit, the emissivity is

$$j_{\nu,high} = \frac{n_e e^2 \nu_B}{c} X_\kappa^{-(\kappa-2)/2}\, sin(\theta)\, 3^{(\kappa-1)/2} \times \frac{(\kappa-2)(\kappa-1)}{4} \Gamma\left(\frac{\kappa}{4} - \frac{1}{3}\right)\Gamma\left(\frac{\kappa}{4} + \frac{4}{3}\right) \tag{D.3}$$

and the absorption coefficient is

$$\alpha_{\nu,high} = \frac{n_e e^2}{\nu m_e c} X_\kappa^{-(1+\kappa)/2} \frac{\pi^{3/2}}{3} \frac{(\kappa-2)(\kappa-1)\kappa}{(\Theta_e\,\kappa)^3} \times \left(\frac{2\Gamma(2+\kappa/2)}{2+\kappa} - 1\right)\left(\left(\frac{3}{\kappa}\right)^{19/4} + \frac{3}{5}\right). \tag{D.4}$$

The final approximations for the emissivity and absorption coefficient are

$$j_\nu = \left(j_{\nu,low}^{-x_j} + j_{\nu,high}^{-x_j}\right)^{-1/x_j} \tag{D.5}$$

$$\alpha_\nu = \left(\alpha_{\nu,low}^{-x_\alpha} + \alpha_{\nu,high}^{-x_\alpha}\right)^{-1/x_\alpha}, \tag{D.6}$$

with $x_j = 3\kappa^{-3/2}$ and $x_\alpha = \left(-\frac{7}{4} + \frac{8}{5}\kappa\right)^{-43/50}$.

The two frequency limits do not have the same dependence on the parameters. The frequency regime is defined by the dimensionless parameter $X_\kappa = \nu/\nu_\kappa$, with $\nu_\kappa = \nu_B(\Theta_e\kappa)^2$. Fig. D.1 shows the relative error of the two regimes (the low frequency in red and the high frequency in blue) compared to the final emission coefficient. While at very high (very low) X_κ, the high-frequency (low-frequency) fitting formulae work very well, there is a large frequency regime ($10^{-2} \lesssim X_\kappa \lesssim 10^3$), hereafter intermediate regime, in which both limits are needed. At 2.2 μm, $X_\kappa > 1$, while $\Theta_e\,\kappa \lesssim 10^3$, which correspond to our typical set of parameters. We therefore used the high-frequency regime to test our EMBLEM.

D.2. Chiaberge & Ghisellini (1999) approximation

It is difficult to model the synchrotron cooling of the electrons with a thermal, power-law, or κ distribution. The evolution of the energy of an electron that emits synchrotron radiation is (e.g., Rybicki & Lightman (1986))

$$\gamma(t) = \gamma_0(1 + A\gamma_0 t)^{-1}, \tag{D.7}$$

$$\text{with } A = \frac{4}{3}\frac{\sigma_T B^2}{8\pi m_e c}, \tag{D.8}$$

γ the Lorentz factor of the electron at time t, and γ_0 the initial Lorentz factor. The energy evolution strongly depends on the initial energy. The higher the initial energy of the electron, the faster its cooling. Thus, the initial distribution we might impose will quickly be deformed (see the top left panel of Fig. 6) and cannot be modeled by one (or more) of the three distribution of Pandya et al. (2016) (thermal, power law, or κ).

In order to properly model the cooling of electrons, we simulated the evolution of the electron distribution with injection and synchrotron cooling (Sect. 3). These simulations yielded the electron distribution $N_e(\gamma, t)$ at different times. We computed the emissivity j_ν and the absorptivity α_ν associated with a range of frequencies from 10^6 to 10^{21} Hz following the formula of Chiaberge & Ghisellini (1999) (with our notation),

$$j_\nu(t) = \frac{1}{4\pi}\int_{\gamma_{min}}^{\gamma_{max}} d\gamma N_e(\gamma, t) P_s(\nu, \gamma), \tag{D.9}$$

and the absorption coefficient follows

$$\alpha_\nu(t) = -\frac{1}{8\pi m_e \nu^2}\int_{\gamma_{min}}^{\gamma_{max}} \frac{N_e(\gamma, t)}{\gamma p}\frac{d}{d\gamma}[\gamma p P_s(\nu, \gamma)], \tag{D.10}$$

where $p = (\gamma^2 - 1)^{1/2}$ is the electron momentum in units of $m_e c$ and P_s is the emissivity of a single electron (see C.3). In order to obtain the emissivity and absorption coefficient at any time and any frequency (to account the relativistic Doppler effect for example), we made a bilinear interpolation.

Appendix E: Analytical approximation for Sgr A* flare peak flux

We derived an analytical expression to compute the time-dependent flux from Sgr A* flares during the growth phase and obtained an analytical formula for the peak flare flux. To do this, we first obtained the approximate analytical form of the varying electron spectrum during the growth phase by solving the kinetic equation, and then computed the approximate synchrotron SED associated with the time-dependent electron spectrum.

E.1. Deriving the time-dependent electron spectrum during the growth phase

The kinetic equation describing the evolution of the electron spectrum during the growth phase is given by Eq. 5,

$$\frac{\partial N_e(\gamma, t)}{\partial t} = \frac{\partial}{\partial \gamma}\left(b_c \gamma^2 N_e(\gamma, t)\right) + Q_{inj}(\gamma, n_e, \theta, \kappa), \tag{E.1}$$

with the injection term $Q_{inj}(\gamma)$ given by Eq. 7 and Eq. 8, and synchrotron cooling term $\dot{\gamma}_{syn} = -b_c(\gamma^2 - 1)$ (see Eq. 6), where $b_c = (4\sigma_T U_B)/(3m_e c)$. We used the approximation $\dot{\gamma}_{syn} \approx -b_c\gamma^2$ because the bulk of the electrons producing the flare emission is highly relativistic. We used the method of characteristics to solve the kinetic equation. We searched for characteristic curves in the γ-t space along which our differential equation in partial derivatives becomes an ordinary differential equation. We rewrite the kinetic equation in the following form, expanding the derivative on the Lorentz factor,

$$\frac{\partial N_e(\gamma, t)}{\partial t} + (-1)b_c\gamma^2\frac{\partial N_e(\gamma, t)}{\partial \gamma} = Q_{inj}(\gamma) + 2\gamma b_c N_e(\gamma, t). \tag{E.2}$$

When we restrict our equation to the characteristic curve ($\gamma(t)$,t), the full derivative of the electron spectrum over time according to the chain rule is

$$\frac{dN_e(\gamma, t)}{dt} = \frac{\partial N_e(\gamma, t)}{\partial t} + \frac{d\gamma}{dt}\frac{\partial N_e(\gamma, t)}{\partial \gamma}. \tag{E.3}$$

Comparing this to Eq. E.2, we identify $(-1)b_c\gamma^2 = \frac{d\gamma}{dt}$, and therefore along the chosen characteristic curve, our equation is split into a system of two ordinary differential equations,

$$\begin{cases} d\gamma/dt = -b_c\gamma^2 \\ dN_e(\gamma, t)/dt = Q_{inj}(\gamma) + 2\gamma b_c N_e(\gamma, t) \end{cases}. \tag{E.4}$$

The solution of the first equation is (applying the initial condition that $\gamma(t = 0) = \xi$)

$$\gamma(t) = \frac{1}{b_c t + 1/\xi}. \tag{E.5}$$

This equation defines a characteristic curve in the γ-t space. We chose the initial point of the characteristic curve as $(\xi, 0)$. The physical meaning of ξ is the initial value of the Lorentz factor of an electron before the cooling process. Eq. E.5 is equivalent to Eq. D.7 and describes how the Lorentz factor of an individual electron evolves in time due to synchrotron cooling. Based on this equation, the initial Lorentz factor ξ is

$$\xi = \xi(\gamma, t) = \frac{1}{1/\gamma - b_c t}. \tag{E.6}$$

This formula defines the initial Lorentz factor of the characteristic curve that passes through a point (γ,t). We denote the function $N_e(\gamma_\xi(t), t) = u(t)$ (electron spectrum along the characteristic curve), and solve the second equation in the system,

$$du/dt - 2b_c\gamma(t)u = Q_{inj}(\gamma(t)), \tag{E.7}$$

The generic solution of this linear differential equation is

$$u(t) = \frac{1}{\mu(t)}\int_0^t \mu(t')\, Q_{inj}(\gamma(t'))\, dt' + \frac{C}{\mu(t)}. \tag{E.8}$$

with C being the integration constant, and the function $\mu(t)$ being the integration factor, which is equal to

$$\mu(t) = \exp\left(\int -2b_c\gamma(t)dt\right) = \frac{1}{(b_c t + 1/\xi)^2}. \tag{E.9}$$

As the electron spectrum at $t = 0$ is zero, we set the initial condition $u(t = 0) = 0$, which results in $C = 0$. Therefore, the solution for $u(t)$ is

$$u(t) = (b_c t + 1/\xi)^2 \int_0^t (b_c t' + 1/\xi)^{-2}\, Q_{inj}(\gamma(t'))\, dt'. \tag{E.10}$$

We return from $u(t)$ to $N_e(\gamma, t)$, which is achieved by substituting the equation for $\xi = \xi(\gamma, t)$ (Eq. E.6) in the expression for

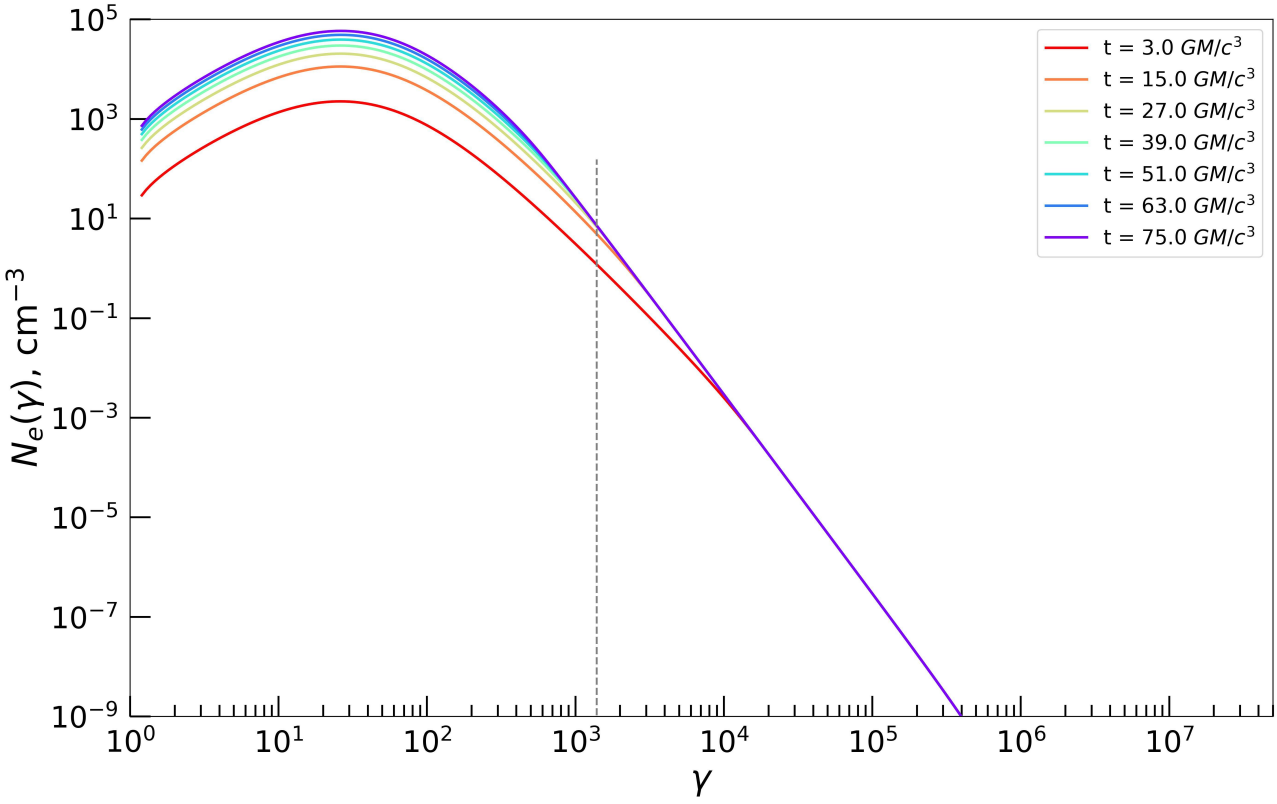

Fig. E.1. Time evolution of the electron distribution with EMBLEM (full lines) from $t = 0$ to $t = t_{\rm growth} = 75\ r_{\rm g}/c$ injecting a κ distribution with $\Theta_{\rm e} = 10$, $\kappa = 4$, and $\dot{n}_{\rm e} = 5.10^6/t_{\rm growth}$. The magnetic field strength is set to 30 Gauss, resulting in a stationary regime for $\gamma > 10^4$ from the very beginning. This regime extends to lower γ values as time growths. To estimate the peak flux, we approximated the whole distribution (at $t = t_{\rm growth}$) by a simple Dirac at $\bar{\gamma}$ represented by the dashed gray line.

$u(t)$. We then obtain an expression for the electron spectrum at a moment of time t,

$$N_{\rm e}(\gamma, t) = \frac{1}{\gamma^2} \int_0^t \Gamma^2\, Q_{\rm inj}(\Gamma)\, dt', \tag{E.11}$$

with $\Gamma = \Gamma(\gamma, t, t') = [1/\gamma + b_c(t' - t)]^{-1}$. We used an approximation for $Q_{\rm inj}(\Gamma)$, and more specifically, for the kappa distribution, to enable analytical integration. In the relativistic regime, and because the peak of the injection spectrum in our case typically occurs at Lorentz factors $\gamma \gg 1$, we can substitute $\gamma(\gamma^2 - 1)^{1/2}$ with γ^2 in the Eq. 8. This leads to some inaccuracies only at very low Lorentz factors, which virtually do not contribute to the integral value and do not contribute to the light-curve flux. We therefore used for the injected spectrum

$$Q_{\rm inj}(\gamma, n_{\rm e}, \theta, \kappa) \approx \frac{N}{t_{\rm growth}} \gamma^2 \left(1 + \frac{\gamma - 1}{\kappa\theta}\right)^{-(\kappa+1)}. \tag{E.12}$$

We then performed the analytical integration. We used the variable substitution from t' to $\Gamma(\gamma, t, t')$. In this case, the differential $dt' = -b_c^{-1}\Gamma^{-2} d\Gamma$. Our integral (Eq. E.11) then becomes

$$N_{\rm e}(\gamma, t) = \frac{N}{\gamma^2 t_{\rm growth}} \int_0^t \Gamma^4 \left(1 + \frac{\Gamma - 1}{\kappa\theta}\right)^{-(\kappa+1)} dt' = \\ = -\frac{N}{b_c \gamma^2 t_{\rm growth}} \int_0^t \Gamma^2 \left(1 + \frac{\Gamma - 1}{\kappa\theta}\right)^{-(\kappa+1)} d\Gamma. \tag{E.13}$$

To solve the integral, we performed the integration by parts, and we obtain

$$\int_0^t \Gamma^2 \left(1 + \frac{\Gamma - 1}{\kappa\theta}\right)^{-(\kappa+1)} d\Gamma = -\frac{\theta\kappa}{(\kappa - 2)(\kappa - 1)} \Psi(\Gamma)\Big|_0^t, \tag{E.14}$$

with

$$\Psi(x) = \left(1 + \frac{x - 1}{\kappa\theta}\right)^{-\kappa} \left[x^2(\kappa - 1) + 2x(\kappa\theta - 1) + 2\theta(\kappa\theta - 2)\right]. \tag{E.15}$$

We substitute the variable back from Γ to t', with $\Gamma(t' = 0) = (1/\gamma - b_c t)^{-1} = \xi(\gamma, t)$ and $\Gamma(t' = t) = \gamma$, and we substitute the expression for the injection spectrum normalization, $N = (1/2) n_{\rm e}(\kappa - 2)(\kappa - 1)\kappa^{-2}\theta^{-3}$ (see Eq. 8) and obtain

$$N_{\rm e}(\gamma, t) = \frac{n_{\rm e}}{2\kappa\theta^2 b_c \gamma^2 t_{\rm growth}} \left[\Psi(\gamma) - \Psi(\xi(\gamma, t))\right]. \tag{E.16}$$

The special case when $b_c t \geq 1/\gamma$ has to be considered separately because this leads to either $\xi \to \infty$ or $\xi < 0$. The second situation is clearly nonphysical because the Lorentz factor cannot be smaller than unity. Qualitatively, $b_c t \geq 1/\gamma \to t \geq 1/(b_c\gamma)$ means that the evolution time of an electron is longer than its cooling timescale, and in this regime, the equilibrium between the injection and cooling is already reached. Therefore, the time-dependent electron spectrum in the Lorentz factor domain $\gamma \geq 1/(b_c t)$ is clearly frozen at the steady-state domain. A steady-state solution corresponds to $\xi \to \infty$, which results in

$\Psi(\xi) \to 0$ (when $\kappa > 2$). Therefore, the final solution for the time-dependent electron spectrum during the growth phase is

$$N_{\rm e}(\gamma, t) = \frac{n_{\rm e}}{2\kappa\theta^2 b_c \gamma^2 t_{\rm growth}} \begin{cases} [\Psi(\gamma) - \Psi(\xi(\gamma, t))], & \text{for } \gamma < (b_c t)^{-1} \\ \Psi(\gamma), & \text{for } \gamma \geq (b_c t)^{-1} \end{cases}. \tag{E.17}$$

The same steady-state solution (the case $\gamma \geq 1/(b_c t)$) might be obtained by directly solving the kinetic equation (Eq. E.1) with $\frac{\partial N_{\rm e}}{\partial t} = 0$. To determine the electron spectrum at the peak of the flare, that is, at the moment when the injection is stopped, we calculate $N_{\rm e}(\gamma, t = t_{\rm growth})$.

E.2. Deriving time-dependent synchrotron SED during the growth phase

We computed the SED and light curve. We used the so-called δ approximation for the electron synchrotron emissivity coefficient. This approximation assumes that a single electron with a Lorentz factor γ emits at a single frequency, rather than a broad spectrum (Rybicki & Lightman 1979),

$$\omega_{\rm peak} \simeq 0.29\omega_c, \tag{E.18}$$

with $\omega_c = 3\gamma^2 eB/(m_{\rm e}c)$ (averaged over pitch angles), e being the electron charge, and B being the magnetic field (CGS units). From this expression, we obtain

$$\nu_{\rm peak} = \frac{\eta e \gamma^2 B}{m_{\rm e} c}, \tag{E.19}$$

where $\eta = (0.29 \times 3)/(2\pi) \approx 0.14$ is a dimensionless numerical factor. For a distribution of electrons, the synchrotron SED in δ approximation is given by (Dermer & Schlickeiser 2002)

$$\nu F_\nu^{\rm syn}(\lambda) = \frac{4}{3}\pi R_b^3 \frac{c\sigma_T U_B}{6\pi D^2} \bar{\gamma}^3 N_{\rm e}(\bar{\gamma}), \tag{E.20}$$

where R_b is the radius of the emitting region, D is the distance between the observer and the source, and $\bar{\gamma}$ is the Lorentz factor of electrons emitting synchrotron photons with a frequency ν. We obtain this Lorentz factor by expressing it from Eq. E.19,

$$\bar{\gamma} = \left(\frac{m_{\rm e} c \nu}{\eta e B}\right)^{1/2}. \tag{E.21}$$

Substituting the expression for $N_{\rm e}(\gamma, t)$ (Eq. E.17), and the expression $b_c = (4\sigma_T U_B)/(3m_{\rm e}c)$ into Eq. E.20, we finally obtained the time-dependent SED during the growth phase in δ approximation,

$$\nu F_\nu^{\rm syn}(\nu, t) = \frac{n_{\rm e} R_b^3 \bar{\gamma} m_{\rm e} c^2}{12 D^2 t_{\rm growth}\, \kappa\theta^2} \begin{cases} [\Psi(\bar{\gamma}) - \Psi(\xi(\bar{\gamma}, t))], & \text{for } \nu < \tilde{\nu}(t) \\ \Psi(\bar{\gamma}), & \text{for } \nu \geq \tilde{\nu}(t) \end{cases}, \tag{E.22}$$

where $\tilde{\nu}(t) = (\eta e B)/(m_{\rm e} c b_c^2 t^2)$ is the frequency corresponding to the condition $\bar{\gamma} = 1/(b_c t)$.

E.3. Evaluating the peak light-curve flux

To obtain a light curve during the growth phase at a specific frequency of interest ν_*, we compute $\mathrm{d}\nu F_\nu^{\rm syn}(\nu = \nu_*, t)$. To compute the peak light curve flux, we evaluated the quantity $\nu F_\nu^{\rm syn}(\nu = \nu_*, t = t_{\rm growth})$.

Appendix F: Additional Setup for the flare on July 22

We also used another setup that reproduced the July 22 flare data well. In this scenario, the magnetic reconnection and so the plasmoid growth phase occurs far before the observing time and the flare is due to the beaming effect combined with the slow decrease of the cooling phase. The peak due to the growth phase occurs during the negative beaming part of the orbit, resulting in a low flux that is comparable to the quiescent state.

Table F.1. Second orbital parameters of the plasmoid model following a conical motion used for the comparison of the July 22 flares observed by GRAVITY Collaboration (2018).

Parameter	Symbol	July 22 bis
Plasmoid		
time in EMBLEM at zero observing time [min]	$t_{obs,0}^{emblem}$	−53
initial orbital radius [GM/c^2]	r_0	15
polar angle [deg]	θ	135
initial azimuthal angle [deg]	φ_0	240
initial radial velocity [c]	$v_{r,0}$	0.01
initial azimthal velocity [rad/s]	$v_{\varphi,0}$	0.047
X position of Sgr A* [μas]	x_0	0
Y position of Sgr A* [μas]	y_0	0
PALN [deg]	Ω	160

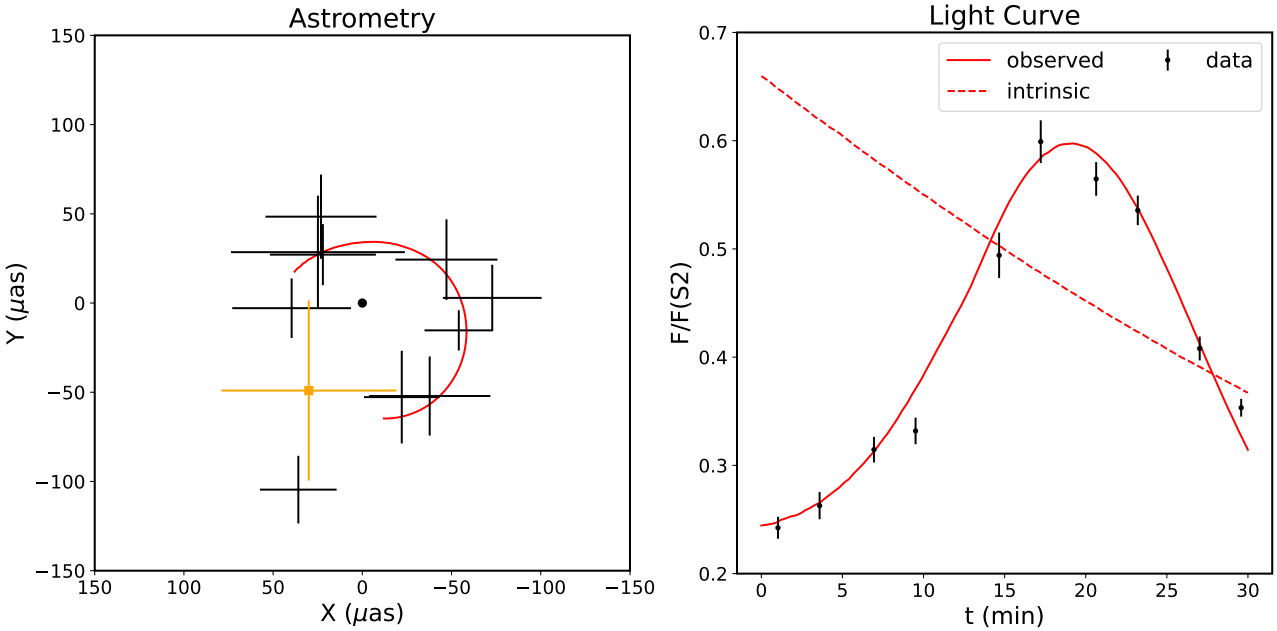

Fig. F.1. Data and plasmoid models of the flares on 22 July 2018. The left panels shows the astrometry of the flare, and the right panel shows the light curves. We used the same setup as in Fig. 8, but with a shorter growth time $t_{\rm growth} = 50 r_{\rm g}/c$, $\Theta_{\rm e} = 72$ and $B = 10$ G (Table F.1), resulting in a two-peak light curve, with the first peak occurring at $t = -22$ min (out of the observational window), but mitigated by the negative beaming effect. The secondary peak, which matched the observed flare data shown here, is due to the positive beaming during the cooling phase (as shown by the intrinsic light curve).